DEVELOPMENT OF STAINLESS CARDIAC HISTOLOGY OF CLINICAL BIOPSY SAMPLES WITH INFRARED SPECTROSCOPY

BY

SAUMYA TIWARI

THESIS

Submitted in partial fulfillment of the requirements
for the degree of Master of Science in Bioengineering
in the Graduate College of the
University of Illinois at Urbana-Champaign, 2017

Urbana, Illinois

Adviser:

Professor Rohit Bhargava

ABSTRACT

Cardiac diseases are the leading cause of mortality in the United States, accounting for every one in seven deaths. There are a large proportion of cardiac diseases that need histopathological examination by pathologists for a conclusive diagnosis, but this technique hasn't been improved upon in the past decade. In this work, we have attempted to advance the current state of histology by developing stainless staining protocols using infrared spectroscopy.

The current gold standard to identify cardiovascular complications such as ischemia, fibrosis, alcoholic cardiomyopathy and transplant rejection is biopsy followed by histology. This approach lacks in many aspects. Major challenges faced by pathologists are: addressing inter-observer variability and experimental variations in stain development, and developing approaches for in-situ histopathology. Specifically, in the case of cardiac transplants, regular monitoring of the transplant is required in order to ensure that the body accepts the transplant. This is done by collecting tissue biopsies at specific time intervals. The presence of lymphocytic infiltration and accompanying fibrosis is indicative of transplant rejection. A prompt clinical action is required if rejection is identified in the biopsy. Cardiac transplant patients can benefit from techniques that can identify lymphocytic infiltration and fibrosis with high accuracy, complementing current pathology practice and giving greater opportunity to pathologists to study complex cases. In the first part of this work, we used infrared spectroscopy coupled with supervised Bayesian classification to identify lymphocytic infiltration and fibrosis in the myocardium in endomyocardial biopsy samples. This classifier was robust and could be easily applied to identify lymphocytes in the tissue and to differentiate between fibrosis in endocardium with fibrosis in myocardium which stains similarly in hematoxylin and eosin stain (H&E).

Repeated biopsy procedures can cause significant trauma to the patient, and often the surgeons require real time histopathology information of the tissue during surgeries. This cannot be accomplished by traditional histology where the tissue sample needs to be excised, sectioned

and stained for analysis. Since infrared spectroscopy in stainless, probe-based instruments can be developed to provide detection *in-situ* but were earlier limited by the speed of imaging using Fourier Transform infrared spectrometers. The problem of speed can be overcome by using quantum cascade laser-based discrete frequency infrared (DFIR) imaging instruments. In the second part of this work, we analyzed data collected on recently developed discrete frequency instruments and compared it to data collected on FT-IR imaging instruments. This was done by unsupervised data clustering to observe histological classes in both types of data.

After establishing that the data collected in DFIR mode retained spectral differences between the histological classes to enable their differentiation, in part three of this work we have done extensive analysis of classification approaches that can be applied to the DFIR data. This study will be relevant to many of the previously built Bayesian classification models that need to be evaluated for their applicability on data collected in discrete frequency mode. In addition, we identified specific spectral features that could be used to differentiate between fibrosis and normal tissue in cardiac biopsy samples computationally at high speed using discrete frequency approach. This can give way to utilization of this model in fiber optic probe-based technology for on-site detection of fibrosis in patients.

ACKNOWLEDGMENTS

I would like to express my deepest gratitude to my advisor, Professor Rohit Bhargava for his guidance and mentoring towards my academic and professional success. Your faith in me propelled me to outperform myself at every stage and continues to do so. I would also extend warm regards to my collaborators who worked with me on this project, as well as my colleagues at Chemical Imaging and Structures lab, for their thoughtful discussions and for sharing their expertise.

I would like to thank my family for always supporting me in all my endeavors. Thank you to my mother, who inspires me to be strong, and to work towards greater good, and my father, who motivates me to achieve excellence at work. Thank you also to my friends, who have been my family and my support away from home.

TABLE OF CONTENTS

INTRODUCTION

Prospects for Chemical Imaging in Cardiovascular Pathology

Abstract

Vibrational Spectroscopy is a well-established technique that utilizes light waves to delineate chemical signatures of samples. The molecular basis of the approach has been well-established for small chemicals and understanding for complex biomedical samples is emerging. In particular, the availability of high-performance and low-cost computation capabilities are now transforming spectroscopic delineation of cellular characteristics in various tissues. This review describes the emergence of this technology and the role it may play in the development of a new way for cardiac tissue assessment at a chemical, molecular and cellular level. The promise in the cardiovascular arena is highlighted with emphasis given to ongoing developments that may transform cardiovascular pathology and imaging.

Current Evaluation of Cardiovascular Diseases and the Need for New Technology

Cardiovascular diseases are the leading cause of mortality in the United States accounting for every one in 7 deaths in the US[1]. Cardiovascular diseases broadly fall into those affecting coronary arteries, valves, cardiac muscle, cardiac rhythm and aortic & vascular structures. There is often overlap of some of these disorders. Patients are frequently imaged through a variety of modalities, which include coronary angiography, echocardiography, computed tomography, magnetic resonance imaging, nuclear scans, conventional x-rays, depending on the type of disorder. However, certain conditions such as diseases affecting the cardiac muscle (cardiomyopathies), cardiac valves (calcification, degeneration, fibrosis, myxomatous changes, infections), cardiac transplant rejection (after heart transplantation), cardiac ischemia/infarction (definitely differentiating between ischemia, infarction, scarring) have been very difficult to diagnose accurately in patients without pathological studies. The use of histopathological examination is confirmatory and the final arbiter in making diagnoses. However, this is

complicated and requires excision or removal of the affected tissue, tissue processing, use of multiple stains and evaluation by experienced pathologists.

The Case for Better Cardiac Assessment

Since the heart is not easily accessible for biopsy, catheter-based techniques have been used to excise small fragments of cardiac tissue, typically from the right ventricle and sometimes from the left ventricle. In the absence of open biopsy of the heart, this is the gold standard for pathological diagnoses. Cores of left ventricular apical muscle during ventricular assist device implants, small off-cuts of outflow tract myocardium in patients undergoing surgical myectomy for HOCM, resected segments of right ventricular muscle in the repair of Tetralogy of Fallot may represent some of the available pathological specimens for analyses.

All of these are invasive to the point of some excision. Non-invasive methods such as angiography, Magnetic resonance imaging (MRI), echocardiography, Computed tomography (CT) scanning, Nuclear Scans show promise but may not correlate with actual pathological states in many conditions. The gold standard continues to be a histopathological evaluation of heart tissue through excisional biopsies of some sort. All of these tests are typically performed as a reactive measure when the patient has symptoms of cardiovascular diseases.

Imaging for CVDs

A variety of clinical tools are used for the assessment and prediction of cardiovascular diseases. Important elements of such tools are described here.

Imaging: Imaging has traditionally been used to identify problematic areas after symptoms have been identified. A number of imaging modalities, such as MRI for assessing ischemic heart disease[2–7] and more recently for quantifying ventricular volume for assessing cardiac function[8] , PET/CT , and SPECT/CT have been used for diagnosis of coronary artery diseases [9–13] and for evaluation of myocardial perfusion[14,15].

Risk factors: Cardiovascular diseases have well-known risk factors among patient populations. For example, conventionally accepted factors such as patient's age[16], family history, dietary

habits, activity levels, diabetes[17], history of smoking, hypertension, and obesity[18,19]; and more recently recognized new generation risk factors such as triglycerides, modified LDL and fibrinogen and levels of C-reactive protein[18,20].

Protein-based biomarkers: Most cardiovascular diseases are progressive and thus, early monitoring and prevention is a viable option for reducing mortality rates. It has been suggested that identification and use of biomarkers related to changes occurring at the molecular stage, before the disease has started showing symptoms can predict the occurrence of disease and outcome[21,22]. Inflammatory markers[23] such as C-reactive protein levels, IL-6, TNF α and IL-10 have been studied as predictors for heart disease risk[24–28]. Blood tests to assess the risk of venous thrombosis and identify possible coagulation of the cardiovascular system have been suggested using markers such as elevated concentrations of factors II, VIII, IX, XI, and fibrinogen[29–32]. Proteins that are present in the heart cells and released after a heart attack, such as Creatine kinase, Myoglobin, Cardiac troponin I etc. can also be measured in the blood to identify myocardial damage[33]. A thorough table enlisting available blood-based tests for heart diseases can be referred to elsewhere[33].

Genetic predisposition: Several genetic abnormalities have been found to be associated with an increased risk of developing cardiovascular disease[34,35]. For example, genetic variation in the lipoprotein A locus is associated with aortic valve calcification[36]; rare de novo copy number variations [37,38]and mutations in GATA4 and TBX5[39] present genetic loci for congenital heart disease. Multiple epigenetic modifications have also been identified that can result in cardiac distress and malfunctions[40–42].

Despite major advances in assessing risk and occurrence of cardiovascular diseases, pathology remains a holdout. In cases requiring histological analysis of tissue, anatomical and physiological changes in diseased states are used. The two major needs are (a) addressing the difficulty of diagnoses in cases, (b) adding molecular information and (c) measuring in situ, living tissue. To address these needs, there are imaging techniques which can probe at the molecular level and identify changes at cellular level much before they are identifiable through conventional techniques. Through molecular imaging, specific molecules, variations in tissues and

extracellular spaces can be identified that could start at the early onset of the disease. In addition, precise identification of the problem at the micro level can enable practitioners to tailor treatment on case by case basis, enabling personalized care.

Molecular imaging for the assessment of cardiovascular diseases

Contrast agent based imaging: Contrast agent based imaging has enabled in vivo probing of abnormalities with currently available imaging modalities. Many developments in this direction have been enabled by emerging nanotechnology-based contrast agents[43,44]. Contrast agents for positron emission tomography (PET) scanning, for example, ^{18}F-FDG have gathered interest as a prospective marker for identification of inflammation[45–47]. However, the clinical applicability of this technique is limited by myocardial uptake of FDG that gives significant signal during PET imaging[48] and efforts are underway to optimize vessel wall imaging using FDG[49,50].

Gadolinium-based contrast agents have been used to target specific sites for detection with MRI[51]. These paramagnetic nanoparticles can get localized to fibrin clots giving high T1 weighted contrast[52]. However, safety concerns arise when using Gd-based contrast agents due to the risk of nephrogenic systemic fibrosis[53]. To counter these, biodegradable polydisulfide dendrimer nanoclusters containing Gd[54] and Manganese based contrast agents are being developed that are expected to reduce such risks[55]. Enhanced uptake of superparamagnetic iron oxide (SPIO) nanoparticles by macrophages has been utilized for identifying macrophage localization. However, a clinical trial utilizing ferucarbotran (Resovist®) did not show any further improvement in visualization of myocardial infarction as compared to the conventional Gd-based imaging modalities[56]. MRI has also emerged as a potential noninvasive technique for detection and quantification of vascular remodeling using elastin-specific MR contrast agents, for which animal models have been studied[57]. Here we have given a short summary of some of the recent developments, readers are referred to specific review articles for an in-depth discussion of targeted molecular imaging agents in the nano and micro size range utilizing conventional imaging modalities[43,58].

Label-free imaging of biological samples: Traditionally, researchers have relied on externally applied contrast agents, such as dyes and fluorescent probes for identification of cell types. In vivo diagnostic tests for many cardiovascular diseases, on the other hand, have utilized the changes in cardiac function to identify the problem using noninvasive techniques. Electrocardiographic (ECG) tests have been long established to assess the electrical activity of the heart and it has been shown that abnormal ECG can be associated with an increased risk of coronary heart disease(CHD) events [59–61] but its utility to predict CHD in asymptomatic adults has not been established yet[62]. It has been difficult to probe at the molecular level in terms of disease diagnosis owing to the limited sensitivity of CT and MRI and limited penetration depth of optical imaging techniques. Conventional techniques have been very effective in the management of a multitude of cardiovascular diseases and do not require extensive modifications. However, amid studying biophysical properties of the tissue/organ and applying the molecular imaging technique for diagnosis by histopathology, there remains a gap between estimation of disease at the surgery table and diagnosis in the pathology lab. The motivation behind developing automated label-free diagnosis techniques is to fill this gap and bring real-time pathology on site. In the following sections of this article, we demonstrate the application of recently developed technology of quantum cascade laser-based infrared imaging for developing automated pathology of cardiovascular diseases and its potential for clinical implementation.

Spectroscopy and its applications in cardiovascular diseases

Spectroscopy pertains to the study of absorption and emission of light waves as it interacts with matter. Various spectroscopic techniques have been utilized in past to probe the structural and biochemical properties of samples based on the wavelength of light used as the probe. Light of radio wave frequency, for example, has been a prime tool for studying molecular structure through magnetic resonance imaging. While near-infrared probes and fluorescence imaging has been explored in great details in past[63–72], optical spectroscopy techniques such as infrared spectroscopy and Raman spectroscopy have not been discussed. Supplementing already developed techniques which can assess myocardial blood flow or perfusion[64,73,74], these techniques are particularly useful for molecular imaging of targets and have become popular to

identify and understand biochemical changes taking place in tissues. Here we will briefly discuss current progress in utilizing these techniques for identification of cardiovascular diseases.

Principles of chemical microscopy and recent enabling advances

Mid-infrared spectroscopy and Raman spectroscopy enable chemical microscopy in the sense that they can quantify chemical constituents and map it on the tissue slide. Therefore, vital macromolecules such as collagen proteins, nucleic acids, and glycogen levels can be analyzed and their distribution of tissue can be assessed. Therefore, these techniques have four-fold potential in assessing cardiovascular diseases. First, mid-infrared chemical imaging can assess collagen level variations in tissue which is correlated with fibrosis. Second, high glycogen levels in tissue are indicative of early ischemia. There is no established way to observe this elevation on tissue section currently but is possible through chemical imaging. Third, apart from identification of high collagen and glycogen levels, infrared microscopy can utilize variation in multiple chemical species present in tissue to digitally stain the tissue without the need of stains. It is, therefore, possible to identify different cell populations present in a tissue section, enabling identification of many cardiovascular diseases, for example, transplant rejection. Fourth, digital pathology data obtained through chemical imaging can be integrated with patient data such as age, weight, and various risk factors to give a personalized diagnosis and prediction of disease outcome. This makes chemical imaging the next generation smart imaging and detection technique with vast potential remaining to be tapped.

Raman spectroscopy

A detailed review has already been written discussing Raman spectroscopy and utilizing it for detection of transplant allograft rejection[75]. In addition, since myocardial infarction and subsequent repair causes significant biochemical changes, it is also possible to observe these changes through Raman spectroscopy[76]. Damage in collagen fiber regions can be analyzed in nondestructive manner[77] and many metabolites such as glucose, cholesterol and lipids can be assessed in the blood which are known risk factors associated with atherosclerotic cardiovascular diseases[78]. A recent study reported high specificity (greater than 98%) and high sensitivity (greater than 96%) in the identification of normal, necrotic, granulated and fibrotic tissue

obtained from rats, establishing label-free Raman spectroscopy to evaluate myocardial infarction[79]. This technique has also been used in past to diagnose coronary atherosclerosis[80–83]. Through optical fiber-based probes, Raman spectroscopy can be used to identify atherosclerosis and monitor its progress, predict plaque rupture and determine therapy[83,84] and such a method can be useful in stainless probing of diseases in situ using Raman spectroscopy.

Mid-infrared spectroscopy

Mid-infrared spectroscopy based disease recognition has been applied in two major cardiovascular fields in past. First is assessing calcifications and characterizing atherlosclerotic plaques to determine vulnerable plaques. In one study, mechanism of aortic valve calcification was elucidated using infrared spectroscopy which showed that amorphous calcium phosphate salts could be detected using infrared spectroscopy which was not analyzable through X-rays[85]. In addition, qualitative and quantitative measurement of lipid content, as well as changes in protein structure in atherosclerotic plaque, can be performed using infrared spectroscopy[86–88]. The water content in tissue can cause strong absorbance in the IR spectrum when tissue is imaged in situ, but water subtraction algorithms can be applied to remove its contribution to characterize atherosclerotic plaques[89,90].

In the second approach, changes in myocardium pertaining with lipids, proteins, and collagen content have been studied using infrared chemical imaging. Wang et al[91] studied hamster models to identify differences in inflammatory response between immune resistant and immuno-permissive mouse models and identified chemical differences between the two in terms of lipid/protein ratio and collagen content. Another study utilized rat models to study collagen deposition post myocardial infarction and identified a strong correlation between FT-IR data and trichrome stain as well as immunohistochemical staining of collagen type I[92]. Studies cited above and others[93] show that extracellular matrix components such as collagen and elastin are crucial to identifying many cardiovascular diseases. Probe-based IR imaging instruments are already being developed and tested on animal models to quantify collagen levels which pave way for in situ studies[94].

Impressive progress has been made in the identification of abnormality in tissues, but such developments have not been sufficient for clinical translation due to (a) the need of high accuracy and (b) ability to image tissue comparable to the gold standard of histopathology. Many *in vivo* techniques have been developed but they fail on the first count and cannot accomplish the second. In some cases, point based detection suffices, but nevertheless, capabilities to perform imaging need to be developed further as they form the basis for future with much greater information content and ability to integrate patient data for greater diagnostic and prognostic accuracy.

In a past study published from our lab, we identified and digitally stained lymphocyte infiltration and fibrosis in endomyocardial biopsy samples from cardiac transplants[95]. Using infrared spectroscopy, high accuracy was obtained when the stain was compared to the pathologists' interpretation of H&E stain. In terms of utility, infrared imaging based stains can significantly reduce the sources of false positives and false negatives during the analysis that can arise from human errors in sample handling, preparation and interpretation. In past, the chief concern in translating this idea to clinics was the speed limitation of conventional infrared imaging systems. However, with the advent of quantum cascade laser (QCL) imaging instruments, imaging specific bands to probe molecular information has become at least 10 times faster. In recent tests conducted in our lab, we found that high accuracy was retained when using QCL for imaging cardiac biopsy samples (unpublished results). This is a huge leap in terms of how samples are analyzed and interpreted currently, and the hope is to develop next generation imaging techniques for rapid detection of diseases using inherent tissue chemistry. Our findings also open up paths to faster and accurate histological analysis of tissues, bringing us closer to the goal of intra-operative and in-vivo imaging.

In conclusion, infrared based chemical imaging has seen major advancements recently with a potential to grow much more. An integrated solution has to be made by jointly considering the benefits and limitations of current and oncoming technologies. A major advantage offered by infrared spectroscopy is the chemical signature of tissue which can be used in conjugation of existing technologies to give a greater level of information associated with the sample. Touch based probes, while in their infancy are being tested and would soon become accessible to the clinics with well-developed computational protocols. Along with capabilities of integrating

patient information and capability of assessing tissue damage real time, this makes infrared spectroscopy a strong candidate for assisting surgeons using intraoperative probes.

References

1. Mozaffarian D, Benjamin EJ, Go AS, et al. Heart Disease and Stroke Statistics-2015 Update: A Report From the American Heart Association. *Circulation* 2014;131(4):e29-322. doi:10.1161/CIR.0000000000000152.

2. Fuster V, Kim RJ. Frontiers in cardiovascular magnetic resonance. *Circulation* 2005;112(1):135-44. doi:10.1161/01.CIR.0000155618.37779.A0.

3. Wang J, Balu N, Canton G, Yuan C. Imaging biomarkers of cardiovascular disease. *J. Magn. Reson. Imaging* 2010;32(3):502-515. doi:10.1002/jmri.22266.

4. Watanabe Y, Nagayama M. MR plaque imaging of the carotid artery. *Neuroradiology* 2010;52(4):253-74. doi:10.1007/s00234-010-0663-z.

5. Corti R, Fuster V. Imaging of atherosclerosis: magnetic resonance imaging. *Eur. Heart J.* 2011;32(14):1709-19b. doi:10.1093/eurheartj/ehr068.

6. Oikawa M, Ota H, Takaya N, Miller Z, Hatsukami TS, Yuan C. Carotid magnetic resonance imaging. A window to study atherosclerosis and identify high-risk plaques. *Circ. J.* 2009;73(10):1765-73.

7. Balu N, Wang J, Dong L, Baluyot F, Chen H, Yuan C. Current techniques for MR imaging of atherosclerosis. *Top. Magn. Reson. Imaging* 2009;20(4):203-15. doi:10.1097/RMR.0b013e3181ea287d.

8. La Gerche A, Claessen G, Van de Bruaene A, et al. Cardiac MRI: a new gold standard for ventricular volume quantification during high-intensity exercise. *Circ. Cardiovasc. Imaging* 2013;6(2):329-38. doi:10.1161/CIRCIMAGING.112.980037.

9. Di Carli MF, Dorbala S, Hachamovitch R. Integrated cardiac PET-CT for the diagnosis and management of CAD. *J. Nucl. Cardiol.* 2006;13(2):139-44.

doi:10.1016/j.nuclcard.2006.02.007.

10. Knaapen P, de Haan S, Hoekstra OS, et al. Cardiac PET-CT: advanced hybrid imaging for the detection of coronary artery disease. *Neth. Heart J.* 2010;18(2):90-8.

11. Kaufmann PA, Di Carli MF. Hybrid SPECT/CT and PET/CT imaging: the next step in noninvasive cardiac imaging. *Semin. Nucl. Med.* 2009;39(5):341-7. doi:10.1053/j.semnuclmed.2009.03.007.

12. Flotats A, Knuuti J, Gutberlet M, et al. Hybrid cardiac imaging: SPECT/CT and PET/CT. A joint position statement by the European Association of Nuclear Medicine (EANM), the European Society of Cardiac Radiology (ESCR) and the European Council of Nuclear Cardiology (ECNC). *Eur. J. Nucl. Med. Mol. Imaging* 2011;38(1):201-12. doi:10.1007/s00259-010-1586-y.

13. Namdar M, Hany TF, Koepfli P, et al. Integrated PET/CT for the Assessment of Coronary Artery Disease: A Feasibility Study. *J. Nucl. Med.* 2005;46(6):930-935.

14. Di Carli MF, Murthy VL. Cardiac PET/CT for the evaluation of known or suspected coronary artery disease. *Radiographics* 2011;31(5):1239-54. doi:10.1148/rg.315115056.

15. Di Carli MF, Dorbala S, Meserve J, El Fakhri G, Sitek A, Moore SC. Clinical myocardial perfusion PET/CT. *J. Nucl. Med.* 2007;48(5):783-93. doi:10.2967/jnumed.106.032789.

16. Lakatta EG. Age-associated Cardiovascular Changes in Health: Impact on Cardiovascular Disease in Older Persons. *Heart Fail. Rev.* 7(1):29-49. doi:10.1023/A:1013797722156.

17. Allison SJ. Cardiovascular disease: progression of coronary artery calcification in patients with type 1 diabetes mellitus with and without kidney disease. *Nat. Rev. Nephrol.* 2013;9(9):494. doi:10.1038/nrneph.2013.142.

18. Wu LL. Review of risk factors for cardiovascular diseases. *Ann. Clin. Lab. Sci.*

29(2):127-33.

19. Mozaffarian D, Wilson PWF, Kannel WB. Beyond established and novel risk factors: lifestyle risk factors for cardiovascular disease. *Circulation* 2008;117(23):3031-8. doi:10.1161/CIRCULATIONAHA.107.738732.

20. Debra L. Parker PCCC, Mary Ann Tucker P, Teresa K. Hoffmann PCCC. Emerging risk factors and risk markers for cardiovascular disease: Looking beyond NCEP ATP III. 2009.

21. Vasan RS. Biomarkers of cardiovascular disease: molecular basis and practical considerations. *Circulation* 2006;113(19):2335-62. doi:10.1161/CIRCULATIONAHA.104.482570.

22. Persidis A. Cardiovascular disease drug discovery. *Nat. Biotechnol.* 1999;17(9):930-1. doi:10.1038/12935.

23. Pearson TA. Markers of Inflammation and Cardiovascular Disease: Application to Clinical and Public Health Practice: A Statement for Healthcare Professionals From the Centers for Disease Control and Prevention and the American Heart Association. *Circulation* 2003;107(3):499-511. doi:10.1161/01.CIR.0000052939.59093.45.

24. Ridker PM. Clinical Application of C-Reactive Protein for Cardiovascular Disease Detection and Prevention. *Circulation* 2003;107(3):363-369. doi:10.1161/01.CIR.0000053730.47739.3C.

25. Ridker PM. Cardiology Patient Page. C-reactive protein: a simple test to help predict risk of heart attack and stroke. *Circulation* 2003;108(12):e81-5. doi:10.1161/01.CIR.0000093381.57779.67.

26. Kritchevsky SB, Cesari M, Pahor M. Inflammatory markers and cardiovascular health in older adults. *Cardiovasc. Res.* 2005;66(2):265-75. doi:10.1016/j.cardiores.2004.12.026.

27. Pai JK, Pischon T, Ma J, et al. Inflammatory markers and the risk of coronary heart

disease in men and women. *N. Engl. J. Med.* 2004;351(25):2599-610. doi:10.1056/NEJMoa040967.

28. Ridker PM, Hennekens CH, Buring JE, Rifai N. C-reactive protein and other markers of inflammation in the prediction of cardiovascular disease in women. *N. Engl. J. Med.* 2000;342(12):836-43. doi:10.1056/NEJM200003233421202.

29. Previtali E, Bucciarelli P, Passamonti SM, Martinelli I. Risk factors for venous and arterial thrombosis. *Blood Transfus.* 2011;9(2):120-38. doi:10.2450/2010.0066-10.

30. Franco RF, Reitsma PH. Genetic risk factors of venous thrombosis. *Hum. Genet.* 2001;109(4):369-84. doi:10.1007/s004390100593.

31. Koster T, Rosendaal FR, Reitsma PH, van der Velden PA, Briët E, Vandenbroucke JP. Factor VII and fibrinogen levels as risk factors for venous thrombosis. A case-control study of plasma levels and DNA polymorphisms--the Leiden Thrombophilia Study (LETS). *Thromb. Haemost.* 1994;71(6):719-22.

32. Kamphuisen PW, Eikenboom JCJ, Bertina RM. Elevated Factor VIII Levels and the Risk of Thrombosis. *Arterioscler. Thromb. Vasc. Biol.* 2001;21(5):731-738. doi:10.1161/01.ATV.21.5.731.

33. Adams J, Apple F. Cardiology patient page. New blood tests for detecting heart disease. *Circulation* 2004;109(3):E12-4. doi:10.1161/01.CIR.0000114134.03187.7B.

34. Kathiresan S, Srivastava D. Genetics of human cardiovascular disease. *Cell* 2012;148(6):1242-57. doi:10.1016/j.cell.2012.03.001.

35. Marian AJ. Recent developments in cardiovascular genetics and genomics. *Circ. Res.* 2014;115(7):e11-7. doi:10.1161/CIRCRESAHA.114.305054.

36. Thanassoulis G, Campbell CY, Owens DS, et al. Genetic associations with valvular calcification and aortic stenosis. *N. Engl. J. Med.* 2013;368(6):503-12. doi:10.1056/NEJMoa1109034.

37. Glessner JT, Bick AG, Ito K, et al. Increased frequency of de novo copy number variants in congenital heart disease by integrative analysis of single nucleotide polymorphism array and exome sequence data. *Circ. Res.* 2014;115(10):884-96. doi:10.1161/CIRCRESAHA.115.304458.

38. Marian AJ. Copy number variants and the genetic enigma of congenital heart disease. *Circ. Res.* 2014;115(10):821-3. doi:10.1161/CIRCRESAHA.114.305243.

39. Misra C, Chang S-W, Basu M, Huang N, Garg V. Disruption of myocardial Gata4 and Tbx5 results in defects in cardiomyocyte proliferation and atrioventricular septation. *Hum. Mol. Genet.* 2014;23(19):5025-35. doi:10.1093/hmg/ddu215.

40. Papait R, Cattaneo P, Kunderfranco P, et al. Genome-wide analysis of histone marks identifying an epigenetic signature of promoters and enhancers underlying cardiac hypertrophy. *Proc. Natl. Acad. Sci. U. S. A.* 2013;110(50):20164-9. doi:10.1073/pnas.1315155110.

41. Papait R, Greco C, Kunderfranco P, Latronico MVG, Condorelli G. Epigenetics: a new mechanism of regulation of heart failure? *Basic Res. Cardiol.* 2013;108(4):361. doi:10.1007/s00395-013-0361-1.

42. Christodoulou DC, Wakimoto H, Onoue K, et al. 5'RNA-Seq identifies Fhl1 as a genetic modifier in cardiomyopathy. *J. Clin. Invest.* 2014;124(3):1364-70. doi:10.1172/JCI70108.

43. Hahn MA, Singh AK, Sharma P, Brown SC, Moudgil BM. Nanoparticles as contrast agents for in-vivo bioimaging: current status and future perspectives. *Anal. Bioanal. Chem.* 2011;399(1):3-27. doi:10.1007/s00216-010-4207-5.

44. Pourmand A, Pourmand MR, Wang J, Shesser R. Application of nanomedicine in emergency medicine; Point-of-care testing and drug delivery in twenty - first century. *Daru* 2012;20(1):26. doi:10.1186/2008-2231-20-26.

45. Bucerius J, Mani V, Wong S, et al. Arterial and fat tissue inflammation are highly

correlated: a prospective 18F-FDG PET/CT study. *Eur. J. Nucl. Med. Mol. Imaging* 2014;41(5):934-45. doi:10.1007/s00259-013-2653-y.

46. Chen W, Dilsizian V. (18)F-fluorodeoxyglucose PET imaging of coronary atherosclerosis and plaque inflammation. *Curr. Cardiol. Rep.* 2010;12(2):179-84. doi:10.1007/s11886-010-0095-8.

47. Hiari N, Rudd JHF. FDG PET imaging and cardiovascular inflammation. *Curr. Cardiol. Rep.* 2011;13(1):43-8. doi:10.1007/s11886-010-0150-5.

48. Saam T, Rominger A, Wolpers S, et al. Association of inflammation of the left anterior descending coronary artery with cardiovascular risk factors, plaque burden and pericardial fat volume: a PET/CT study. *Eur. J. Nucl. Med. Mol. Imaging* 2010;37(6):1203-12. doi:10.1007/s00259-010-1432-2.

49. Bucerius J, Mani V, Moncrieff C, et al. Optimizing 18F-FDG PET/CT imaging of vessel wall inflammation: the impact of 18F-FDG circulation time, injected dose, uptake parameters, and fasting blood glucose levels. *Eur. J. Nucl. Med. Mol. Imaging* 2014;41(2):369-83. doi:10.1007/s00259-013-2569-6.

50. Chen W, Kim J, Molchanova-Cook OP, Dilsizian V. The potential of FDG PET/CT for early diagnosis of cardiac device and prosthetic valve infection before morphologic damages ensue. *Curr. Cardiol. Rep.* 2014;16(3):459. doi:10.1007/s11886-013-0459-y.

51. Friedrich MG, Strohm O, Schulz-Menger J, Marciniak H, Luft FC, Dietz R. Contrast Media Enhanced Magnetic Resonance Imaging Visualizes Myocardial Changes in the Course of Viral Myocarditis. *Circulation* 1998;97(18):1802-1809. doi:10.1161/01.CIR.97.18.1802.

52. Flacke S, Fischer S, Scott MJ, et al. Novel MRI Contrast Agent for Molecular Imaging of Fibrin: Implications for Detecting Vulnerable Plaques. *Circulation* 2001;104(11):1280-1285. doi:10.1161/hc3601.094303.

53. Reiter T, Ritter O, Prince MR, et al. Minimizing risk of nephrogenic systemic fibrosis in

cardiovascular magnetic resonance. *J. Cardiovasc. Magn. Reson.* 2012;14:31. doi:10.1186/1532-429X-14-31.

54. Huang C-H, Nwe K, Al Zaki A, Brechbiel MW, Tsourkas A. Biodegradable polydisulfide dendrimer nanoclusters as MRI contrast agents. *ACS Nano* 2012;6(11):9416-24. doi:10.1021/nn304160p.

55. Pan D, Schmieder AH, Wickline SA, Lanza GM. Manganese-based MRI contrast agents: past, present and future. *Tetrahedron* 2011;67(44):8431-8444. doi:10.1016/j.tet.2011.07.076.

56. Yilmaz A, Rösch S, Klingel K, et al. Magnetic resonance imaging (MRI) of inflamed myocardium using iron oxide nanoparticles in patients with acute myocardial infarction - preliminary results. *Int. J. Cardiol.* 2013;163(2):175-82. doi:10.1016/j.ijcard.2011.06.004.

57. von Bary C, Makowski M, Preissel A, et al. MRI of coronary wall remodeling in a swine model of coronary injury using an elastin-binding contrast agent. *Circ. Cardiovasc. Imaging* 2011;4(2):147-55. doi:10.1161/CIRCIMAGING.109.895607.

58. McAteer MA, Choudhury RP. Targeted molecular imaging of vascular inflammation in cardiovascular disease using nano- and micro-sized agents. *Vascul. Pharmacol.* 2013;58(1-2):31-8. doi:10.1016/j.vph.2012.10.005.

59. Auer R, Bauer DC, Marques-Vidal P, et al. Association of major and minor ECG abnormalities with coronary heart disease events. *JAMA* 2012;307(14):1497-505. doi:10.1001/jama.2012.434.

60. De Bacquer D, De Backer G, Kornitzer M, Blackburn H. Prognostic value of ECG findings for total, cardiovascular disease, and coronary heart disease death in men and women. *Heart* 1998;80(6):570-577. doi:10.1136/hrt.80.6.570.

61. Kannel WB, Kannel C, Paffenbarger RS, Cupples LA. Heart rate and cardiovascular mortality: The Framingham study. *Am. Heart J.* 1987;113(6):1489-1494.

doi:10.1016/0002-8703(87)90666-1.

62. Moyer VA. Screening for coronary heart disease with electrocardiography: U.S. Preventive Services Task Force recommendation statement. *Ann. Intern. Med.* 2012;157(7):512-8. doi:10.7326/0003-4819-157-7-201210020-00514.

63. Frangioni J. In vivo near-infrared fluorescence imaging. *Curr. Opin. Chem. Biol.* 2003;7(5):626-634. doi:10.1016/j.cbpa.2003.08.007.

64. Nakayama A, del Monte F, Hajjar RJ, Frangioni J V. Functional near-infrared fluorescence imaging for cardiac surgery and targeted gene therapy. *Mol. Imaging* 2002;1(4):365-77.

65. Chen J, Tung C-H, Allport JR, Chen S, Weissleder R, Huang PL. Near-infrared fluorescent imaging of matrix metalloproteinase activity after myocardial infarction. *Circulation* 2005;111(14):1800-5. doi:10.1161/01.CIR.0000160936.91849.9F.

66. Schenke-Layland K, Riemann I, Stock UA, König K. Imaging of cardiovascular structures using near-infrared femtosecond multiphoton laser scanning microscopy. *J. Biomed. Opt.* 2005;10(2):024017. doi:10.1117/1.1896966.

67. Moreno PR. Detection of Lipid Pool, Thin Fibrous Cap, and Inflammatory Cells in Human Aortic Atherosclerotic Plaques by Near-Infrared Spectroscopy. *Circulation* 2002;105(8):923-927. doi:10.1161/hc0802.104291.

68. Jaffer FA, Tung C-H, Wykrzykowska JJ, et al. Molecular imaging of factor XIIIa activity in thrombosis using a novel, near-infrared fluorescent contrast agent that covalently links to thrombi. *Circulation* 2004;110(2):170-6. doi:10.1161/01.CIR.0000134484.11052.44.

69. Gardner CM, Tan H, Hull EL, et al. Detection of lipid core coronary plaques in autopsy specimens with a novel catheter-based near-infrared spectroscopy system. *JACC. Cardiovasc. Imaging* 2008;1(5):638-48. doi:10.1016/j.jcmg.2008.06.001.

70. Waxman S, Dixon SR, L'Allier P, et al. In vivo validation of a catheter-based near-infrared spectroscopy system for detection of lipid core coronary plaques: initial results of the SPECTACL study. *JACC. Cardiovasc. Imaging* 2009;2(7):858-68. doi:10.1016/j.jcmg.2009.05.001.

71. Hilderbrand SA, Weissleder R. Near-infrared fluorescence: application to in vivo molecular imaging. *Curr. Opin. Chem. Biol.* 2010;14(1):71-9. doi:10.1016/j.cbpa.2009.09.029.

72. Jaffer FA, Calfon MA, Rosenthal A, et al. Two-dimensional intravascular near-infrared fluorescence molecular imaging of inflammation in atherosclerosis and stent-induced vascular injury. *J. Am. Coll. Cardiol.* 2011;57(25):2516-26. doi:10.1016/j.jacc.2011.02.036.

73. Tanaka E, Chen FY, Flaumenhaft R, Graham GJ, Laurence RG, Frangioni J V. Real-time assessment of cardiac perfusion, coronary angiography, and acute intravascular thrombi using dual-channel near-infrared fluorescence imaging. *J. Thorac. Cardiovasc. Surg.* 2009;138(1):133-40. doi:10.1016/j.jtcvs.2008.09.082.

74. Sevick-Muraca EM. Translation of near-infrared fluorescence imaging technologies: emerging clinical applications. *Annu. Rev. Med.* 2012;63:217-31. doi:10.1146/annurev-med-070910-083323.

75. Tu Q, Chang C. Diagnostic applications of Raman spectroscopy. *Nanomedicine* 2012;8(5):545-58. doi:10.1016/j.nano.2011.09.013.

76. Huser T, Chan J. Raman spectroscopy for physiological investigations of tissues and cells. *Adv. Drug Deliv. Rev.* 2015;89:57-70. doi:10.1016/j.addr.2015.06.011.

77. Votteler M, Carvajal Berrio DA, Pudlas M, Walles H, Stock UA, Schenke-Layland K. Raman spectroscopy for the non-contact and non-destructive monitoring of collagen damage within tissues. *J. Biophotonics* 2012;5(1):47-56. doi:10.1002/jbio.201100068.

78. Borges R de CF, Navarro RS, Giana HE, Tavares FG, Fernandes AB, Silveira Junior L.

Detecting alterations of glucose and lipid components in human serum by near-infrared Raman spectroscopy. *Res. Biomed. Eng.* 2015;31(2):160-168. doi:10.1590/2446-4740.0593.

79. Nishiki-Muranishi N, Harada Y, Minamikawa T, et al. Label-free evaluation of myocardial infarction and its repair by spontaneous Raman spectroscopy. *Anal. Chem.* 2014;86(14):6903-10. doi:10.1021/ac500592y.

80. Buschman HP, Motz JT, Deinum G, et al. Diagnosis of human coronary atherosclerosis by morphology-based Raman spectroscopy. *Cardiovasc. Pathol.* 10(2):59-68.

81. Buschman HP, Deinum G, Motz JT, et al. Raman microspectroscopy of human coronary atherosclerosis: biochemical assessment of cellular and extracellular morphologic structures in situ. *Cardiovasc. Pathol.* 10(2):69-82.

82. Peres MB, Silveira L, Zângaro RA, Pacheco MTT, Pasqualucci CA. Classification model based on Raman spectra of selected morphological and biochemical tissue constituents for identification of atherosclerosis in human coronary arteries. *Lasers Med. Sci.* 2011;26(5):645-55. doi:10.1007/s10103-011-0908-z.

83. van de Poll SWE, Römer TJ, Puppels GJ, van der Laarse A. Imaging of atherosclerosis. Raman spectroscopy of atherosclerosis. *J. Cardiovasc. Risk* 2002;9(5):255-61.

84. Römer TJ, Brennan JF, Fitzmaurice M, et al. Histopathology of human coronary atherosclerosis by quantifying its chemical composition with Raman spectroscopy. *Circulation* 1998;97(9):878-885.

85. Dritsa V, Pissaridi K, Koutoulakis E, Mamarelis I, Kotoulas C, Anastassopoulou J. An infrared spectroscopic study of aortic valve. A possible mechanism of calcification and the role of magnesium salts. *In Vivo* 2014;28:91-8.

86. P. Wrobel T, Mateuszuk L, Chlopicki S, Malek K, Baranska M. Imaging of lipids in atherosclerotic lesion in aorta from ApoE/LDLR−/− mice by FT-IR spectroscopy and Hierarchical Cluster Analysis. *Analyst* 2011;136:5247. doi:10.1039/c1an15311k.

87. Kodali DR, Small DM, Powell J, Krishnan K. Infrared Micro-imaging of Atherosclerotic Arteries. *Appl. Spectrosc.* 1991;45:1310-1317. doi:10.1366/0003702914335878.

88. Wrobel TP, Majzner K, Baranska M. Protein profile in vascular wall of atherosclerotic mice analyzed ex vivo using FT-IR spectroscopy. *Spectrochim. Acta - Part A Mol. Biomol. Spectrosc.* 2012;96:940-945. doi:10.1016/j.saa.2012.07.103.

89. Manoharan R, Baraga JJ, Rava RP, Dasari RR, Fitzmaurice M, Feld MS. Biochemical analysis and mapping of atherosclerotic human artery using FT-IR microspectroscopy. *Atherosclerosis* 1993;103:181-193. doi:10.1016/0021-9150(93)90261-R.

90. Baraga JJ, Feld MS, Rava RP. Detection of Atherosclerosis in Human Artery by Mid-Infrared Attenuated Total Reflectance. *Appl. Spectrosc.* 1991;45(4):709-711. doi:10.1366/0003702914337047.

91. Wang Q, Sanad W, Miller LM, et al. Infrared imaging of compositional changes in inflammatory cardiomyopathy. *Vib. Spectrosc.* 2005;38(1-2):217-222. doi:10.1016/j.vibspec.2005.02.011.

92. Cheheltani R, Wang B, Sabri A, Pleshko N, Kiani M. Fourier transform infrared imaging spectroscopy of collagen deposition after myocardial infarction. In: *2012 38th Annual Northeast Bioengineering Conference (NEBEC)*. IEEE; 2012:305-306. doi:10.1109/NEBC.2012.6207086.

93. Yang TT, Weng SF, Zheng N, et al. Histopathology mapping of biochemical changes in myocardial infarction by Fourier transform infrared spectral imaging. *Forensic Sci. Int.* 2011;207(1-3):e34-9. doi:10.1016/j.forsciint.2010.12.005.

94. Cheheltani R, McGoverin CM, Rao J, Vorp DA, Kiani MF, Pleshko N. Fourier transform infrared spectroscopy to quantify collagen and elastin in an in vitro model of extracellular matrix degradation in aorta. *Analyst* 2014;139(12):3039-47. doi:10.1039/c3an02371k.

95. Tiwari S, Reddy VB, Bhargava R, Raman J. Computational chemical imaging for

cardiovascular pathology: chemical microscopic imaging accurately determines cardiac transplant rejection. *PLoS One* 2015;10(5):e0125183. doi:10.1371/journal.pone.0125183.

CHAPTER 1

Computational Imaging for Cardiovascular Pathology: Chemical Microscopic Imaging Accurately Determines Cardiac Transplant Rejection[1]

Abstract

Rejection is a common problem after cardiac transplants leading to significant number of adverse events and deaths, particularly in the first year of transplantation. The gold standard to identify rejection is endomyocardial biopsy. This technique is complex, cumbersome and requires a lot of expertise in the correct interpretation of stained biopsy sections. Traditional histopathology cannot be used actively or quickly during cardiac interventions or surgery. Our objective was to develop a stain-less approach using an emerging technology, Fourier transform infrared (FT-IR) spectroscopic imaging to identify different components of cardiac tissue by their chemical and molecular basis aided by computer recognition, rather than by visual examination using optical microscopy. We studied this technique in assessment of cardiac transplant rejection to evaluate efficacy in an example of complex cardiovascular pathology. We recorded data from human cardiac transplant patients' biopsies, used a Bayesian classification protocol and developed a visualization scheme to observe chemical differences without the need of stains or human supervision. Using receiver operating characteristic curves, we observed probabilities of detection greater than 95% for four out of five histological classes at 10% probability of false alarm at the cellular level while correctly identifying samples with the hallmarks of the immune response in all cases. The efficacy of manual examination can be significantly increased by observing the inherent biochemical changes in tissues, which enables us to achieve greater diagnostic confidence in an automated, label-free manner. We developed a computational pathology system that gives high contrast images and seems superior to traditional staining

[1] Reprinted, with permission, from Saumya Tiwari, Vijaya B. Reddy, Rohit Bhargava, and Jaishankar Raman. "Computational Chemical Imaging for Cardiovascular Pathology: Chemical Microscopic Imaging Accurately Determines Cardiac Transplant Rejection."PloS one 10, no. 5 (2015): e0125183. doi:10.1371/journal.pone.0125183

procedures. This study is a prelude to the development of real time *in situ* imaging systems, which can assist interventionists and surgeons actively during procedures.

Introduction

The success of cardiac transplantation depends foremost on the immune response to the new implant[1]. The gold standard for identifying allograft rejection is endomyocardial biopsy (EMB)[2]. Endomyocardial biopsy section from a normal heart consists mostly of myocardium which is unoriented and appears red-tan. The tissue section is bordered by the overlying endocardium which is pearly white in appearance[3]. In case of cardiac transplant, an activation of the immune system can cause severe inflammation which can result in transplant rejection and eventual death of patient. Grade of acute cellular rejection, as defined by the revised ISHLT (International Society for Heart & Lung Transplantation) heart biopsy grading scale[4] is determined by the presence of infiltrate and associated myocyte damage. Grade 0 signifies no rejection while grade 2 (mild rejection), 3 (moderate rejection) and 4 (severe rejection) requires assessing the number of foci of infiltrate and associated myocardium damage. Prolonged tissue damage, which could be a result of immune attack, injury or toxins etc. may result in deposition of extracellular matrix components at the site of damage, leading to a condition termed as fibrosis[5-7]. Such an observation of fibrosis is important in assessing myocardium damage in case of allograft rejection. For a detailed description of histopathology associated with cardiac allograph rejection, the readers are directed to available literature[3-5].

In routine cases of monitoring allograft reception, biopsy sections are stained and the inflammatory response is observed, which is predominantly lymphocytic[3]. This approach suffers from inter-observer variability and an inability to quantify accuracy and confidence in data[8-9]. The estimation variance complicates decision-making. For example, misinterpretation of fibrosis through the sub-endocardium can give the erroneous impression of extensive fibrosis[2] and can cause false positives. The subjective nature of histopathological assessment and the apparent potential for errors has long been recognized and debated upon[10-11]. This has led to development of immunohistochemistry for diagnostic purposes by evaluation of specific biomarkers[11-12] but this technique can get affected from variations in sample preparation, fixation procedures, antibody specificity and similar other experimental details[12] .There is a need, therefore, to explore

technologies that can make routine histopathological examinations more accurate, consistent, facile and reliable.

As opposed to the standard practice of staining tissue with dyes or molecular imaging of specific epitopes, the emerging technology of chemical imaging can utilize the inherent molecular contrast within samples to provide histologic data. One approach in particular, infrared (IR) spectroscopic imaging, offers strong contrast, high sensitivity and rapid data recording. It has shown potential broadly in biomedical applications for understanding metabolomics and molecular diagnostics[13-14]. Combined with computer algorithms, IR imaging has been used for differentiating between diverse cell types in tissues and for detecting disease[15-17]. Several studies related to cardiovascular systems have reported spectral analysis of tissue and disease in terms of resulting biochemical changes. Infrared imaging has been used to study calcifications in aortic valve[18], for characterizing heart valves[19], studying diabetes induced changes in myocardium and vessels[20-23], for analyzing cardiac extracellular matrix (ECM) remodeling[24]; and ECM and serum components following myocardial infarction[25-28]. While these studies successfully demonstrate differentiation between diseased and healthy tissue via lipid and protein composition and collagen content, a histologic analysis consistent with existing pathology practice is lacking. Characterization of atherosclerotic plaques[29-35] is a step towards clinically-actionable information. However, a practical assay to diagnose conditions and provide actionable information is still lacking. One step in this direction is to utilize digital information obtained from FT-IR spectroscopy and develop a classification protocol which can assign cell identifier value to each pixel on the tissue image. Such classification systems, which require multivariate analysis have been attempted for identification of various cell types in cancer but very little work is found in diseases related to heart[36-37]. Specifically in case of identification of cardiac allograft rejection, we require an automated detection system that has ability to distinguish not only between different cell types but more importantly correctly identify lymphocytes. Identification of lymphocytes is also critically needed as it has potential importance in assessment of many more diseases, for example, identification of tumor infiltrating lymphocytes is also of great interest, and a recent study has sought to identify lymphocytic signature in peripheral blood samples[38]. Another study has utilized unsupervised clustering algorithm to obtain impressive identification of B and T cells in a single patient sample using infrared spectroscopy[39]. However,

when analyzing multiple patient samples, accounting for point-to-point variations in the samples and across samples is difficult via unsupervised classifications, leading to reduction in accuracy. The work presented in this manuscript takes this goal of identifying lymphocytes one step further by classifying infiltrating lymphocytes spatially in a biopsy section using supervised classification algorithms of infrared spectroscopy data. Given the complexity and expertise required when conventional pathology is used to diagnose transplant rejection in the heart, we used chemical imaging to see if it could provide the necessary diagnoses and visualizations useful in clinical practice. We utilized differences in the infrared absorbance patterns among different histological classes to develop an automated system where the digital input of IR spectroscopy data yielded a computationally colored image showing different classes similar to what one would obtain using rigorous staining procedures.

Materials and methods

Sample procurement

Written consent was obtained in all patients for study of their archived pathological specimens. The consents were recorded and maintained securely and separately. The consent process for this study was reviewed by the IRB at Rush University Medical Center and approved. All specimens were anonymized, de-identified and no clinical or demographic information was recorded. Thirty five anonymized human EMB sections from ten patients, formalin fixed and paraffin embedded were examined. The biopsies were taken using a bioptome, which is an instrument inserted through the internal jugular vein, and directed under fluoroscopy to be positioned in the right ventricle. The biopsies are then taken as small pieces of tissue, typically measuring 1 mm x 1 mm x1 mm. The section thickness was 5μm. Of the thirty five sections obtained; three sections had to be discarded due to damage to the sections. Out of the 10 patients analyzed, patient 1-5 had no rejection; thus counted as control. Patient 6, 7 and 8 had moderate rejection; and patient 9 and 10 had mild rejection. In current practice, it is very rare to find samples with grade 4 severe rejection, and hence such samples could not be included in the study.

Sample preparation

Samples were microtomed onto reflective low-emission (Low-E) glass slides for IR imaging. These slides provide a reflective substrate for the sample in IR light but are transparent to visible light. Although when using Low-E slides, the IR beams pass through the sample twice and suffers from distortions in the spectrum[40-41], we have observed that standard preprocessing and treatment of data yields good classification results without performing rigorous corrections for distortions. Albeit using substrates like Calcium Fluoride and Barium Fluoride is preferable, Low-E slides are inexpensive and easy to maintain, making them more practical in clinical environment. Prior to acquiring IR data, paraffin was removed from the samples by washing them twice with hexane and immersion in hexane for 14 hours at room temperature with continuous stirring. Removal of paraffin was evident from the reduction of paraffin-associated CH bending peak at 1464cm^{-1} (fig. 1). Furthermore, the spectral features used in our analysis were extracted from regions which are not affected by paraffin vibrational modes to ensure that any residual paraffin did not interfere with results.

Fourier transform infrared imaging

De-paraffinized sections were imaged under mid-infrared light on the IR imaging system. FT-IR imaging was performed using a Spotlight 400 system from Perkin Elmer. Spectra were collected using a liquid nitrogen cooled mercury-cadmium-telluride (MCT) 16-element linear array detector. The background was collected on a clear area of low-E slide at 4cm^{-1} resolution using 120 scans for each sample. All images were acquired in reflection mode with 6.25 µm x 6.25 µm pixel size and 4 cm^{-1} spectral resolution with 2cm^{-1} step size using a single interferometer scan with signal to noise ratio (SNR) exceeding 500:1 in all cases. Data was collected over the mid-infrared region and truncated for storage (800cm^{-1} to 4000cm^{-1}). The image resolutions were nominally 6.25 µm and 25 µm. Since the samples were large, (smallest dimension being at least 500 µm for every section) and irregularly shaped, each image was acquired by breaking it down to 5-10 smaller rectangular regions and using raster scanning of these parts. Each region was separately focused by the instrument to remove any error due to

change in focus and the composite image was stitched back together using ENVI-IDL 4.8(Environment for Visualizing Images-Interactive Data Language). Processing time for a square section of 1mm X 1mm at 6.25 µm, starting with imaging and obtaining computational stain was about 2 hours. Processing time for the same section at 25 µm was about 10 minutes. It has to be kept in mind that this imaging was performed by sweeping through all the wavenumber bands from 4000 cm^{-1} to 800 cm^{-1} at 4 cm^{-1} resolution. After building the classifier, one can realize that only a segment of this range is actually necessary for classification (discussed in results), and thus scanning at discrete frequencies for detection can enable reduction in imaging time by three folds or larger[42-43].

Hematoxylin and Eosin (H&E) staining

Serial sections were preserved and stained with H&E for initial determination of rejection grade by the pathologist. In addition, after IR imaging was performed on sections, the sections on low-E slides were stained with Hematoxylin and Eosin stains for future comparisons and imaged using Zeiss visible microscope. All the data analysis done in this manuscript used H&E images from same section imaged by infrared spectroscopy and not serial section.

Data analysis

Data pre-processing: Acquired data were imported in ENVI-IDL 4.8 software for analysis. A figure annotating important IR peak assignment is shown in supplementary figure 1. A very comprehensive table of band assignments of IR spectra of heart tissue is given in this study[20] which can also be referred to. Throughout the analysis, we excluded pixels without protein-characteristic Amide I absorbance since all cells and ECM in this tissue will contain protein (see fig. 1). This was done by setting a threshold of minimum absorbance value corresponding to an absorbance of 0.30, which is at least 10-fold larger than the peak-to-peak noise in the data.

Identification of histological features (classes): With the aim of understanding spectral differences in various components of the section and in order to build a Bayesian classifier for

automated classification of the sections, we first built a classification grid comprising of 16 sections by combining data from 16 images in a single file. The breakdown of 16 chosen sections for classification training set was as follows: 3 sections from patient 1, 2 sections each from patient 5, 6,9,10 and 1 section each from patient 2, 3, 4, 7, and 8. Sections were chosen to sufficiently represent each class, namely Myocardium, Endocardium, Fibrosis (Endocardium), Fibrosis (Myocardium) and Lymphocytes and to provide maximum inter-patient diversity to the training set. Remaining sections were used for validation set. The breakdown of validation set was as follows: 2 sections each from patient 3, 4, 5, 6, 7, 8, and 9 and 1 section each from patient 1 and 10.

We then used the peak height of vibrational mode at 1236 cm^{-1} to see contrast between lymphocytes and muscle. The 1236 cm^{-1} peak is associated with CH_2 wagging vibrations associated with proteins[44-45]; which was found to be useful in prima facie differentiation of different classes (see fig. 2). Five histological classes, namely, Myocardium, Endocardium, Fibrosis (Endocardium), Fibrosis (Myocardium) and Lymphocytes were considered for our analysis. After H&E staining of samples, regions were marked by pathologist as the above classes and this annotation was considered as gold standard[46]. Next, exact same regions were marked in IR images by comparison with pathologist-annotated H&E images from same sections. Care was taken to mark only those regions which clearly belonged to a particular class as seen from H&E images (gold standard, as described earlier[46]). This process yielded approximately 330,000 spectra for training the classification algorithm. For each of the classes, a linear two point correction across peaks of interest or specific peaks was used. The points were fixed for all spectra in the sample. Spectra were normalized to amide I peak (1652 cm^{-1}) to account for the variations in sample thickness[47]. We then extracted average spectra for each class, which is shown in fig. 1.

Bayesian classification algorithm: Our Bayesian classifier works by determining the likelihood that an unknown pixel belongs to a particular class by using biochemically significant features called metric parameters defined by the user. Each of these parameters can have different weights in the classification process depending on their ability to differentiate between classes. We used a protocol that has previously been established and validated[44,48,49]. Using the spectral differences

observed among the classes in training set (shown in fig. 1), we defined a set of 217 parameters using four types of spectral metrics (peak height ratio, peak area to height ratio, peak area to area ratio and center of gravity) to differentiate each class from the others. To begin with, normalized peak heights are considered as parameters for all peaks appearing in absorbance spectrum using peak height ratio with amide I peak. Next, other quantities, peak area to height ratio, peak area to area ratio and center of gravity are defined as metric parameters using peaks in the spectra by manual examination of the differences in spectra between classes. This gave us 217 metric parameters to analyze data with. The significance of these metrics is to reduce data to significant quantities which is readily analyzable[44].

Use of ratios instead of absolute values also ensures that these metric definitions are independent of variability in instrumentation and sample preparation steps. We evaluated these metrics in terms of their ability to separate the classes by using minimum error in identification of class and the area under the curve (AUC) for the Receiver Operating Characteristic (ROC). We further tested the Bayesian classifier built using these parameters on an independent set of sections to evaluate its accuracy in identification of classes. The findings are described in the following section.

Results and discussion

Training

Samples were imaged using IR microscopy and correlated to features in H&E images that were marked by the pathologist's review as the ground truth. Computerized pattern recognition of IR imaging data from unstained EMB samples led to every tissue pixel being classified into a specific histological class. Compared to the ground truth, the resultant probability of detection at the pixel level for the training set was quite high for lymphocytes (0.991), fibrosis-endocardium (0.999), fibrosis-myocardium (0.997) and myocardium (0.952) and somewhat lower for endocardium (0.860) with approximately 0.10 probability of false alarm (fig 3 (i)). There is a probability of confusing fibrosis with endocardium as evident from confusion matrix shown in table 1. As can be seen, 48.5% of the tissue identified as endocardium by the pathologist was

classified as fibrosis in myocardium and 9.1% of the endocardium was identified as fibrosis in endocardium. It is well known that the nature and structure of endocardium is not well visualized with conventional pathological methods. This may be due to endocardial damage caused by the bioptome and the fact that endocardium is a very thin layer that is easily washed away during preparation. The lower accuracy in this data set also arises from a limited number of endocardium pixels, as partly mitigated by having higher number of pixels in validation set (supplementary table 1). The issue of endocardium damage during biopsy is unfortunately out of our control. The nature of the biopsy is such that as the bioptome is used along the endocardial surface of the right ventricle, there is inherent damage to the endocardium. This coupled with the fact that the endocardium is a thin, evanescent layer that is easily damaged/disturbed makes endocardial evaluation difficult. Therefore, we have not discussed any precautions for sample preparation. It is important to remember that findings pathognomonic of transplant rejection are not manifested in the endocardium but in the sub-endocardial tissue and in the myocardium. Since our focus here was the identification of transplant rejection, future efforts can be undertaken to refine the data and potentially improve efficiency by better capability instruments for enhanced spatial resolution and faster imaging time. Focused efforts to collect specific tissue components, such as endocardium would give us sample size large enough to accurately characterize these components.

Validation

We performed validation using an independent set of 16 samples with approximately 300,000 pixels. Uniformly high probability of detection with low probability of false alarm (0.13) was found (fig 3(ii)). Comparison of our technique with H&E staining is shown in fig. 4; and comparison from different grades of rejection has been shown for boxed areas from figure 4 in Supplementary figure 2. Probability of detection at 10% probability of false alarm is provided in table 2. While achieving significant accuracy, our approach is likely limited by mixed pixels (particularly in regions of lymphocyte infiltration; which is strongly associated with myocyte necrosis and fibrosis) and inclusion of boundary pixels. This limitation is also reflected in identification of endocardium for which we do not have comparatively good representation of

pure pixels. Endocardium was not easily visible in the pathology specimens either. While pixel level accuracy may be improved, we achieved accurate identification of the key histopathologic features for decision-making in every sample. Hence, we sought to examine if accurate information could be achieved by speeding up the data acquisition process. Scanning at coarser resolutions can not only make chemical imaging real time but may also lead to higher accuracy due to the higher signal to noise ratio of the detector[50]. Hence, we also collected data at a larger pixel size of 25µm x 25µm (at least 16-fold faster) to evaluate the applicability of the procedure at lower resolution. As seen from fig. 3(iii) and fig. 4, most classes are identified well, but the confidence in data reduces due to larger pixel size. This leads to lower sensitivity which is typical of tradeoff between time required to take image and the resolution achieved[48]. We anticipate that a multi-scale scanning algorithm will be practical when translated to use. The tissue could be scanned in minutes at low resolution and specific areas can be scanned at higher resolution for better accuracy. It is notable that the molecular basis of our histologic approach provides this flexibility, and is truly unique to this technology as we have deployed. In contrast, morphologic analysis of conventional stained tissue is specific to the resolution and is very unlikely to yield similar results. The ability to identify areas of concern with coarse resolution and hone into those areas with high resolution maybe analogous to scanning at low power and then searching the involved areas with high power microscopy. However, the FT-IR imaging based approach is significantly quicker and may be automated quite easily. Presence of lymphocytes in endocardium as well as in nearby myocardium can be checked by looking up neighbors of pixels using simple algorithms; which could also enable us to quantitate foci of infiltrations used for grading rejection. Future efforts can be undertaken to incorporate these ideas and making IR based detection a practical technique by using focal plane array (FPA) detectors for high spatial resolution at faster time frames by utilizing noise reduction[51] techniques.

Infrared imaging to identify chemical changes in tissue

According to the ISHLT criteria[4], for the sample to be qualified as grade zero (no rejection), there should be no evidence of mononuclear inflammation or myocyte damage. We observed that in all grade 0 cases, there were negligible lymphocyte pixels, and even the lymphocytes that were

found were not encroaching in the myocardium. Thus, using IR spectroscopy, it is very straightforward to differentiate between positive (rejected) and negative (not rejected) samples. In addition to histologic identification, biochemical changes undergone by tissues can also be captured using chemical imaging. Since our hypothesis was that the classifier could capture important tissue changes efficiently, we have related specific infrared absorption patterns that we identified from the classifier with previous observations. During fibrosis, ECM components (majorly collagen) are accumulated in the myocardium[52] which is apparent by higher infrared absorption intensity of amide III peak in fibrotic regions[53]. Our classifier correspondingly identified the absorbance at 1236 cm^{-1} (high contribution from collagen[15,45,49,54] as an important parameter(Table 3 and table 4). Peak due to absorbance at 1236 cm^{-1} / 1239 cm^{-1} is due to the CH_2 wagging vibrations associated with proteins and is known as amide III peak. However, for the sample being analyzed here, owing to empirical evidences (Fig 2(i)) and observations from past literature discussed above, it can be inferred that major contribution to this peak is coming from collagen. With peaks at 1204 cm^{-1} and 1239 cm^{-1} reflecting the characteristic vibrational modes of collagen proteins-amide III[55] (fig. 2 (i)), a significantly low level was observed in healthy myocardium. Absorbance (1027 cm^{-1} to 1032 cm^{-1}) associated with glycogen[56] was decreased at sites of fibrosis (fig. 2 (iii)) as previously noted[57]. Hence, this multivariate approach, utilizing multiple biochemical characteristics of tissues, is effective in identifying multiple pathologic conditions.

Together, these results indicate that both the spatial and chemical information can be utilized to identify tissue changes during immune response to the allograft. While we use cardiac allograft rejection as a proof of concept, chemical imaging can be expanded to identify additional cardiac pathologic conditions. Studies show that the false negative rate in identification of myocarditis can be up to 45% due to errors in sampling and sensitivity[58]. Differentiation of lymphocytes from other normal constituents like mast cells, fibroblast nuclei, pericytes and endothelial cells is difficult via visual pathological examination[59]. It has already been shown that IR spectroscopy can identify different cell types[16,60,61]. However, it has been very difficult to classify lymphocytes using earlier supervised classifiers due to low density of lymphocytes in other tissues, and their small size, resulting in problems of mixed pixels at current spatial resolution. It is possible to quantify lymphocyte infiltration in tissue in terms of number of pixels per sample. Supplementary

table 1 shows the number of pixels marked for each class using gold standard. About 83% of these were correctly identified as lymphocytes by our classifier. This data can be combined with quantification of associated myocyte damage in order to computationally assess the grade of rejection. We are confident that using high definition IR imaging systems[62,63] would enable us to differentiate between even more cell types, making this technique very useful for pathology applications in a variety of conditions.

While manual examination would require presence of lymphocytes in the section (resulting in error due to sampling as well as need to sample multiple times from patient), infrared spectroscopy can potentially detect changes undergone by the tissue which are indicative of transplant rejection even when lymphocytes are not picked in sampling, reducing the error rates, false negatives and avoiding significant trauma to the patient tissue. Apart from chemical information associated with tissues, tissues digitally stained with IR imaging approach are capable of providing a much better contrast and easy quantification of lymphocytes which can greatly reduce the time and effort spent per section by the pathologist.

This report stresses the capabilities of this approach in a complex condition such as cardiac transplant rejection, which traditionally needs careful tissue preparation, multiple stains and review by experienced cardiac pathologists to provide accurate diagnoses. Combined with the speed of the data acquisition and emerging technologies for high speed IR microscopy[42,43], we believe this study opens the path to more rapid tissue assessment much closer to the patient than previously possible. Eventually, intra-operative and *in vivo* imaging can be attempted based on chemical molecular imaging. This can be made possible by touch probe based fiber optic technology on which work is currently under progress. Multiple studies show that spectral in-vivo analysis is promising using probe based instruments and have previously been applied to study atherosclerosis [64-66] and to detect cancer[67-68]. Using attenuated total reflectance (ATR) infrared imaging, mid-infrared light can be used to detect the ailment. Moreover, since this study has already identified specific molecular peaks that can be used for detection, we can now build instruments that operate on discrete frequencies to give even faster detection systems. This is different from near-infrared imaging, which has many pitfalls in making accurate diagnoses[69].

Although the present study has shown excellent promise in terms of on-site detection, we are currently limited by spatial resolution and speed of data acquisition and processing. Spatial resolution used in this study can identify single lymphocytes larger than 10 μm, and lymphocytes smaller than this can be identified in large enough cluster. While the current study can successfully identify grade 0 through grade 4, in order to accurately identify grade 2(mild rejection), one would require much better spatial resolution to identify single lymphocytes. This task can be accomplished in near future using high definition imaging systems which have spatial resolution of the order of single micron, reducing the problem of boundary pixels and enabling us to identify every cell more accurately in tissue. Another challenge faced by pathologists is to identify whether the rejection is cellular or antibody mediated. Good spatial resolution is necessary to identify individual cells and to classify cells that are present in low density in tissues, for example macrophages, basophils; or bacterial cells in case of pathogen infections. As the project expands, we hope to be able to identify many other cell populations in the region such as activated mononuclear cells and pathogens; making spectroscopic analysis of specific cells possible. This could in turn enable us to understand other pathological mechanisms of disease development. While we were limited by speed in terms of imaging and data processing in this study, progress is now being made to reduce data acquisition time by manifolds using discrete infrared spectroscopy[42,43]. The trade-off between the resolution and time can also be improved by the use of FPA detectors, using which large areas can be measured at higher resolutions at faster time frames, and which are becoming more and more amenable. These advances further go on to show that IR imaging provides a potential approach for next generation histology procedures that are highly precise and accurate while the automation can lead to better decision making closer to the patient. This could be done within a very short period of time; thereby reducing the work load on pathologist and bringing smart detection devices to surgery suites.

Conclusion

The chemical molecular imaging approach offers numerous advantages over traditional sample examination techniques, providing a new avenue for clinical diagnosis. Chemical information, along with morphologic and architectural tissue information provides for a comprehensive

analysis of tissue. Computer algorithms allow us to dispense with staining and pathological recognition is aided by color coded images. In this study, we have shown an example of how chemical imaging can be applied in cardiac tissues to achieve automated pathology while providing a high probability of detection and low probability of false alarm. We identified specific spectral characteristics which related to the biochemical changes undergone by the tissue which could be used for chemical detection of rejection. In future, we can make this even more extensive by differentiating between acute cellular rejection and Quilty lesions. This is the first study to show that the chemical molecular imaging approach can be used to diagnose complex cardiac conditions, with results equivalent to and probably superior to conventional pathology.

This technique would also be useful in identifying other cell populations that can be present in cardiovascular environment such as activated immune cells, antibody mediated rejection and bacterial infections to name a few. It is also possible to integrate this digital data with patient history to provide an even more nuanced scientific assessment of disease and prognosis. The idea here is to kick start the development of an approach which can give an all-encompassing rapid diagnosis at the site of collection of sample without stains and more importantly, assist during surgery for identification of diseased and problem areas in the heart & vasculature.

Acknowledgements

The corresponding author certifies that no other persons besides the authors have made substantial contributions to this manuscript.

Figures and Tables

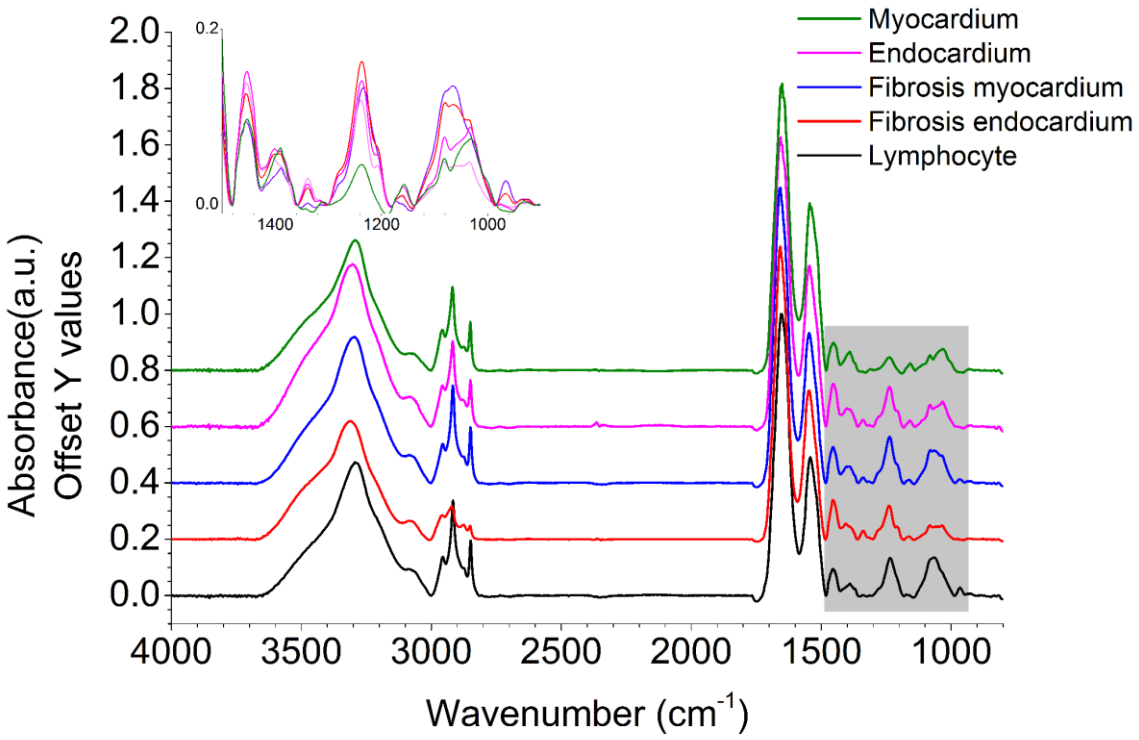

Figure 1: Baseline corrected absorption spectra, normalized using the Amide I peak, for all five classes of cells observed in the study. Important spectral differences observed over the fingerprint spectral region (1500-900 cm^{-1}) are highlighted in grey and zoomed in without offset.

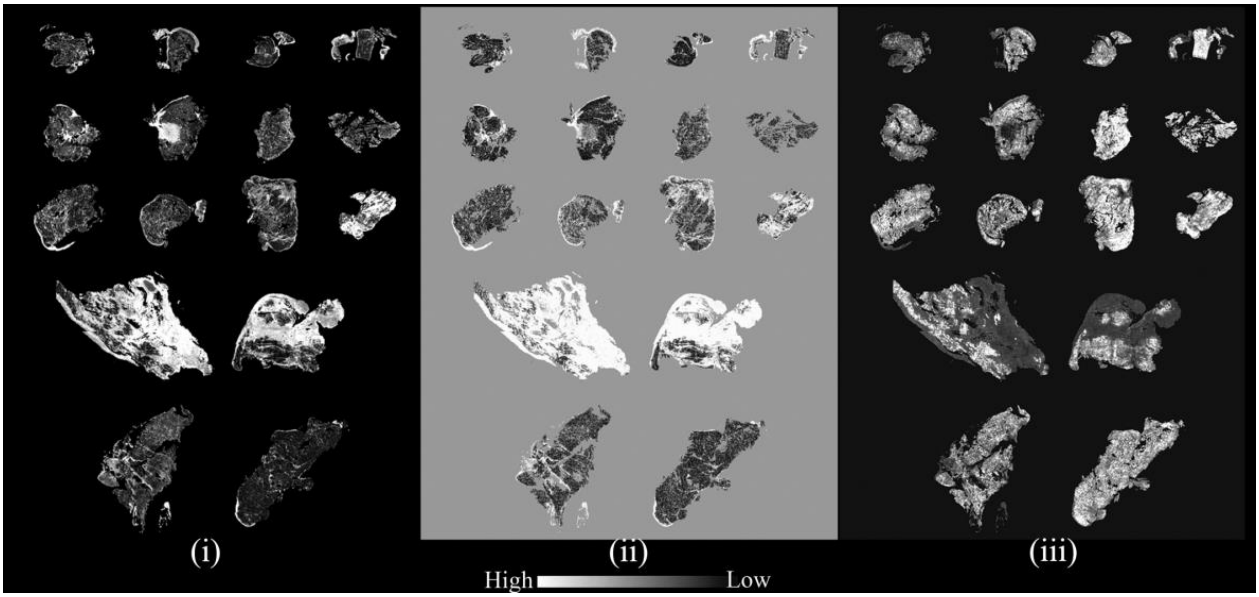

Figure 2: Relative intensities of peak height ratios useful in discriminating classes; examples from metric definitions (i) 1239cm^{-1} to 1652cm^{-1}; (ii) 1204cm^{-1} to 1236cm^{-1}; (iii) 1027cm^{-1} to 1543cm^{-1}

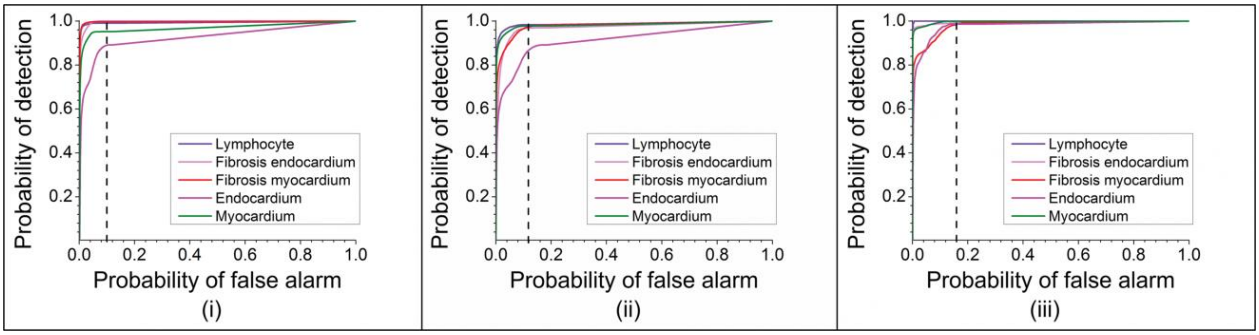

Figure 3: Receiver operating characteristic (ROC) curves demonstrating the accuracy of the classification algorithm (i) Training set at 6.25 µm x 6.25 µm pixel size; (ii) Validation set at 6.25 µm x 6.25 µm pixel size; (iii) Validation set at 25 µm x 25 µm pixel size

Table 1: Confusion matrix for classification for validation data and training data (in parentheses)

	Ground Truth(Percentage)				
Class	Endocardium	Myocardium	Lymphocyte	Fibrosis myocardium	Fibrosis endocardium
Unclassified	3.10 (10.90)	2.25 (4.80)	1.68 (0.90)	1.87 (0.30)	2.21 (0.10)
Endocardium	**12.74** (12.30)	0.08 (0.20)	0.00 (0.00)	1.28 (0.30)	0.55 (0.80)
Myocardium	6.42 (18.90)	**95.91** (94.50)	0.03 (0.50)	10.11 (0.40)	0.02 (0.00)
Lymphocyte	0.19 (0.40)	0.02 (0.00)	**82.82** (85.70)	4.74 (13.20)	0.00 (0.00)
Fibrosis myocardium	52.91 (48.50)	1.54 (0.50)	15.48 (12.90)	**81.49** (84.80)	3.53 (19.10)
Fibrosis endocardium	24.65 (9.10)	0.20 (0.00)	0.00 (0.00)	0.49 (1.10)	**93.69** (80.00)
Total	100	100	100	100	100

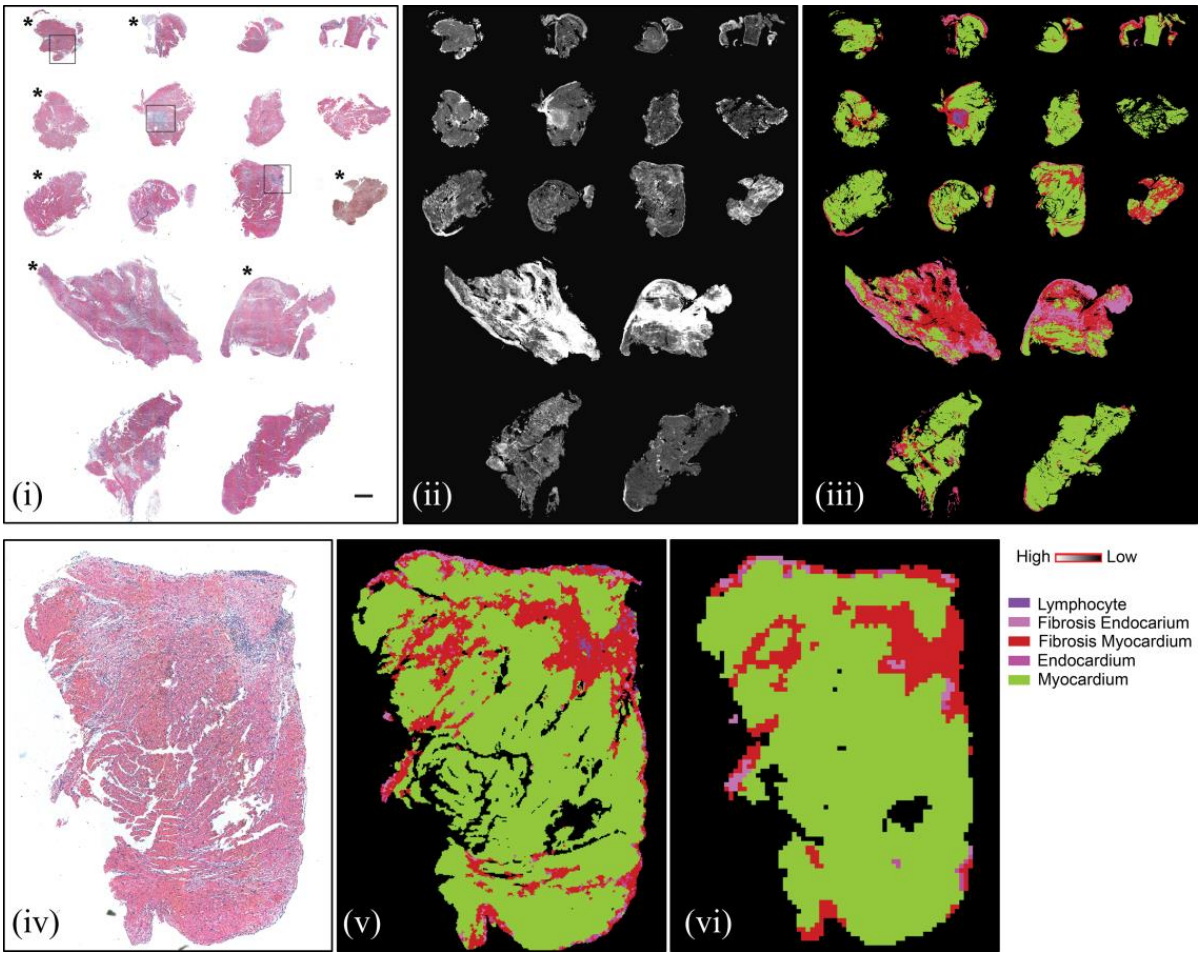

Figure 4: Biopsy section array of 16 samples used for validation. Top panel: (i) H&E stained image of sections (scale bar represents 500µm); Asterisk marked samples showed no rejection in pathologist review. (ii) absorbance at 1236 cm^{-1} demonstrating differences between samples and different cell types; (iii) Classified IR image showing color coded pixels indicating different pathological classes; Bottom panel: Magnified view of one sample from validation set with matched lower spatial resolution IR image. (iv) H&E stained image of section; (v) Classified 6.25 µm x 6.25 µm pixel size IR image; (vi) Classified 25 µm x 25 µm pixel image.

Table 2: Probability of detection at 10% probability of false alarm

	Training	Validation 6.25 µm	Validation 25µm
Lymphocyte	99.1	98.3	72.9
Fibrosis endocardium	99.9	95.7	93.3
Fibrosis myocardium	99.7	95.9	62
Endocardium	86	85.8	48.4
Myocardium	95.2	97.5	88.7

Table 3: List of metric definitions found useful to differentiate classes- peak height ratio; all values are in wavenumber (cm^{-1})

Peak Height Ratio		Peak Height Ratio		Peak Height Ratio	
Peak 1	Peak 2	Peak 1	Peak 2	Peak 1	Peak 2
1389	1236	3315	1236	1204	1236
1027	1065	1163	1236	1239	1652
1239	1543	1163	1065	1236	1543
1389	1452	1452	1543	1236	3300
1239	3300	1389	1652	1389	3300
1389	1065	1452	1236	1027	1543
1405	1236	1155	1452	1032	1236

Table 4: List of metric definitions found useful to differentiate classes- peak area to height ratio and center of gravity; all values are in wavenumber (cm^{-1})

Peak area to peak height ratio			Center of gravity			
Left area bound	Right area bound	Peak position	Left bound	Right bound	CG 1	CG 2
1482	1594	1652	1184	1302	1188	1216
1424	1480	1546	1482	1726	1482	1594
1184	1300	1652	984	1144	1016	1048

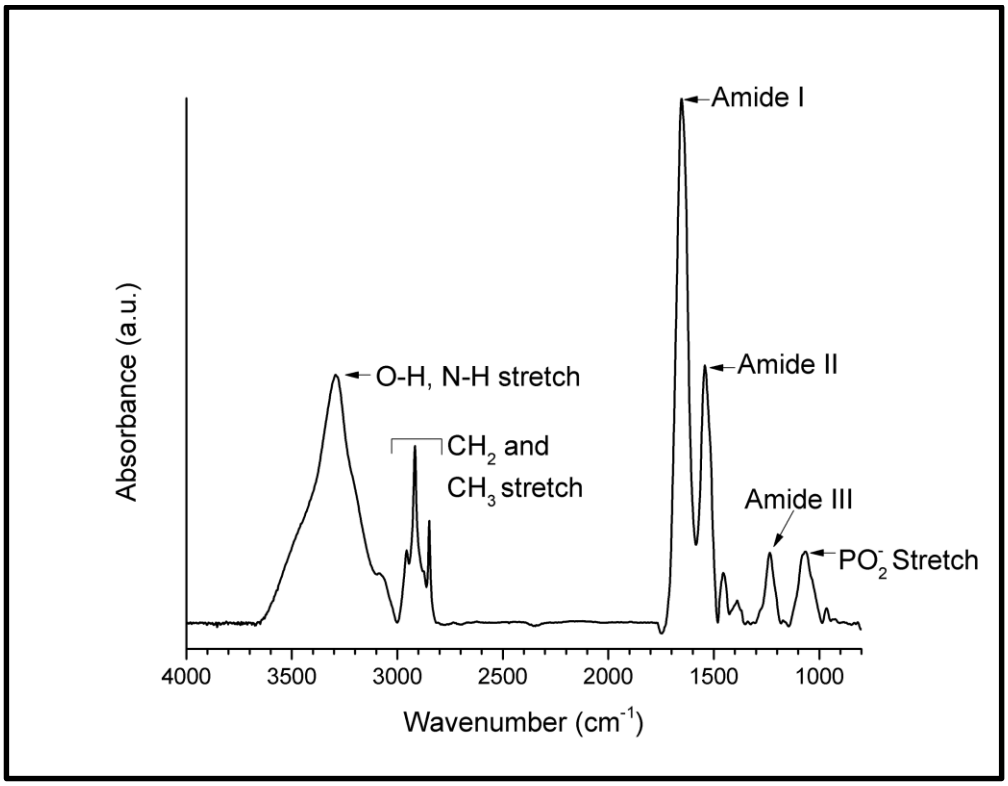

Figure 5: IR peak assignments for tissue

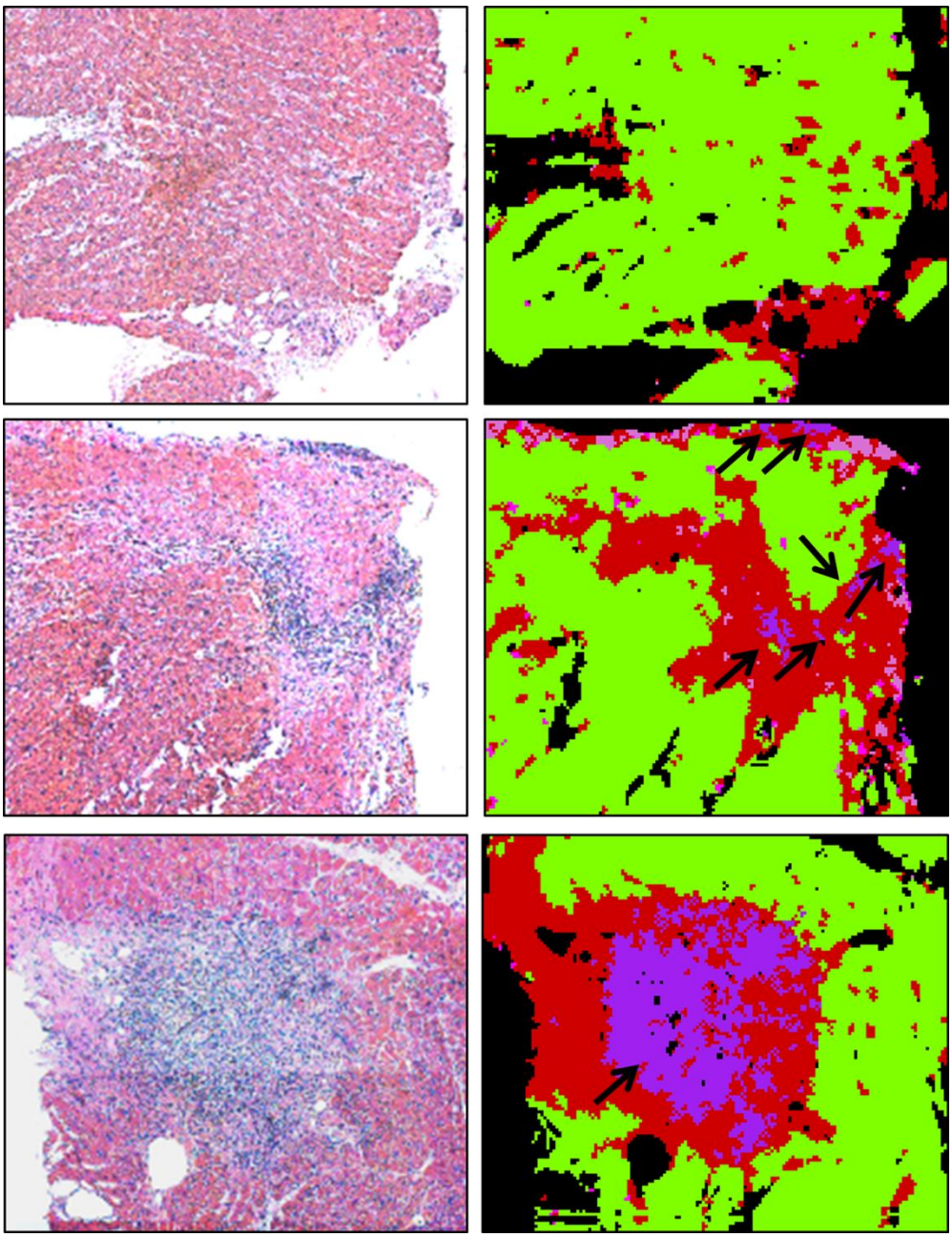

Figure 6: Computationally stained infrared image compared with H&E image at various grades of rejection. Arrows show lymphocytic infiltration. Top panel: No rejection; Middle panel: Mild rejection; Bottom panel: Moderate rejection.

Table 5: Number of pixels for each class in training and validation sets

	Training	Validation
Myocardium	218024	229001
Endocardium	3508	4317
Lymohocyte	18671	3219
Fibrosis Myocardium	11904	18158
Fibrosis Endocardium	77287	51848

References

1. Patel JK, Kittleson M, Kobashigawa J a. Cardiac allograft rejection. Surgeon. Elsevier Ltd; 2011;9: 160–7. doi:10.1016/j.surge.2010.11.023

2. Fenoglio JJ, Marboe CC. Endomyocardial biopsy: an overview. Hum Pathol. WB Saunders; 1987;18: 609–612.

3. Stone JR, Basso C, Baandrup UT, Bruneval P, Butany J, Gallagher PJ, et al. Recommendations for processing cardiovascular surgical pathology specimens: a consensus statement from the Standards and Definitions Committee of the Society for Cardiovascular Pathology and the Association for European Cardiovascular Pathology. Cardiovasc Pathol. Elsevier Inc.; 2012;21: 2–16. doi:10.1016/j.carpath.2011.01.001

4. Stewart S, Winters G, Fishbein M, Tazelaar H, Kobashigawa J, Abrams J, et al. Revision of the 1990 working formulation for the standardization of nomenclature in the diagnosis of heart rejection. J Hear Lung Transplant. 2005;24: 1710–20. doi:10.1016/j.healun.2005.03.019

5. Lange LG, Schreiner GF. Mechanisms of disease. N Engl J Med. 1994;330: 1129–1135.

6. Friedman SL. Mechanisms of disease: Mechanisms of hepatic fibrosis and therapeutic implications. Nat Clin Pract Gastroenterol Hepatol. 2004;1: 98–105. doi:10.1038/ncpgasthep0055

7. Kumar V, Abbas AK, Fausto N, Aster J. Tissue Renewal, Regeneration, and Repair. Pathologic Basis of Disease. 8th ed. Philadelphia: Elsevier; 2010. pp. 79–110.

8. Shanes JG, Ghali J, Billingham ME, Ferrans VJ, Fenoglio JJ, Edwards WD, et al. Interobserver variability in the pathologic interpretation of endomyocardial biopsy results. Circulation. 1987;75: 401–405. doi:10.1161/01.CIR.75.2.401

9. Hahn E a, Hartz VL, Moon TE, O'Connell JB, Herskowitz a, McManus BM, et al. The Myocarditis Treatment Trial: design, methods and patients enrollment. Eur Heart J. 1995;16 Suppl O: 162–167.

10. Edwards WD. Current problems in establishing quantitative histopathologic criteria for the diagnosis of lymphocytic myocarditis by endomyocardial biopsy. Heart Vessels Suppl. 1985;1: 138–142. doi:10.1007/BF02072381

11. Hammond MEH, Stehlik J, Snow G, Renlund DG, Seaman J, Dabbas B, et al. Utility of histologic parameters in screening for antibody-mediated rejection of the cardiac allograft: A study of 3,170 biopsies. J Hear Lung Transplant. 2005;24: 2015–2021. doi:10.1016/j.healun.2005.08.014

12. Walker R a. Quantification of immunohistochemistry - Issues concerning methods, utility and semiquantitative assessment I. Histopathology. 2006;49: 406–410. doi:10.1111/j.1365-2559.2006.02514.x

13. Ellis DI, Goodacre R. Metabolic fingerprinting in disease diagnosis: biomedical applications of infrared and Raman spectroscopy. Analyst. 2006;131: 875–85. doi:10.1039/b602376m

14. Petrich W. Mid-infrared and raman spectroscopy for medical diagnostics. Appl Spectrosc Rev. 2001;36: 181–237. doi:10.1081/A

15. Holton SE, Walsh MJ, Kajdacsy-Balla a, Bhargava R. Label-free characterization of cancer-activated fibroblasts using infrared spectroscopic imaging. Biophys J. Biophysical Society; 2011;101: 1513–21. doi:10.1016/j.bpj.2011.07.055

16. Walsh MJ, Reddy RK, Bhargava R, Member A. Label-Free Biomedical Imaging With Mid-IR Spectroscopy. IEEE J Sel Top quantum Electron. 2012;18: 1502–1513.

17. Nallala J, Piot O, Diebold M-D, Gobinet C, Bouché O, Manfait M, et al. Infrared imaging as a cancer diagnostic tool: introducing a new concept of spectral barcodes for identifying molecular changes in colon tumors. Cytometry A. 2013;83: 294–300. doi:10.1002/cyto.a.22249

18. Dritsa V, Pissaridi K, Koutoulakis E, Mamarelis I, Kotoulas C, Anastassopoulou J. An infrared spectroscopic study of aortic valve. A possible mechanism of calcification and the role of magnesium salts. In Vivo. 2014;28: 91–8.

19. Jastrzebska M, Zalewska-Rejdak J, Mróz I, Barwinski B, Wrzalik R, Kocot a, et al. Atomic force microscopy and FT-IR spectroscopy investigations of human heart valves. Gen Physiol Biophys. 2006;25: 231–244.

20. Toyran N, Lasch P, Naumann D, Turan B, Severcan F. Early alterations in myocardia and vessels of the diabetic rat heart: an FTIR microspectroscopic study. Biochem J. 2006;397: 427–436. doi:10.1042/BJ20060171

21. Toyran N, Severcan F, Severcan M, Turan B. Investigation of diabetes-induced effect on apex of rat heart myocardium by using cluster analysis and neural network approach: An FTIR study. Spectroscopy. 2007;21: 269–278. doi:10.1155/2007/269618

22. Majzner K, Wrobel TP, Fedorowicz A, Chlopicki S, Baranska M. Secondary structure of proteins analyzed ex vivo in vascular wall in diabetic animals using FT-IR spectroscopy. Analyst. 2013;138: 7400–10. doi:10.1039/c3an00455d

23. Birarda G, Holman E a, Fu S, Weikel K, Hu P. Synchrotron infrared imaging of advanced glycation endproducts (AGEs) in cardiac tissue from mice fed high glycemic diets. Biomed Spectrosc Imaging. 2013;2: 301–315. doi:10.3233/BSI-130057

24. Gough KM, Zelinski D, Wiens R, Rak M, Dixon IMC. Fourier transform infrared evaluation of microscopic scarring in the cardiomyopathic heart: Effect of chronic AT1 suppression. Anal Biochem. 2003;316: 232–242. doi:10.1016/S0003-2697(03)00039-3

25. Cheheltani R, Wang B, Sabri A, Pleshko N, Kiani M. Fourier Transform Infrared Imaging Spectroscopy of Collagen Deposition after Myocardial Infarction. Bioengineering Conference (NEBEC), 2012 38th Annual Northeast. IEEE; 2012. pp. 305–306.

26. Petrich W, Lewandrowski KB, Muhlestein JB, Hammond MEH, Januzzi JL, Lewandrowski EL, et al. Potential of mid-infrared spectroscopy to aid the triage of patients with acute chest pain. Analyst. 2009;134: 1092–1098. doi:10.1039/b820923e

27. Wetzel DL, Post GR, Lodder R a. Synchrotron infrared microspectroscopic analysis of collagens I, III, and elastin on the shoulders of human thin-cap fibroatheromas. Vib Spectrosc. 2005;38: 53–59. doi:10.1016/j.vibspec.2005.02.029

28. Lui K, Jackson M, Sowa MG, Ju H, Dixon IM, Mantsch HH. Modification of the extracellular matrix following myocardial infarction monitored by FTIR spectroscopy. Biochim Biophys Acta. 1996;1315: 73–7.

29. Manoharan R, Baraga JJ, Rava RP, Dasari RR, Fitzmaurice M, Feld MS. Biochemical analysis and mapping of atherosclerotic human artery using FT-IR microspectroscopy. Atherosclerosis. 1993;103: 181–193. doi:10.1016/0021-9150(93)90261-R

30. Baraga JJ, Feld MS, Rava RP. Detection of Atherosclerosis in Human Artery by Mid-Infrared Attenuated Total Reflectance. Appl Spectrosc. 1991;45: 709–711. doi:10.1366/0003702914337047

31. P. Wrobel T, Mateuszuk L, Chlopicki S, Malek K, Baranska M. Imaging of lipids in atherosclerotic lesion in aorta from ApoE/LDLR−/− mice by FT-IR spectroscopy and Hierarchical Cluster Analysis. Analyst. 2011;136: 5247. doi:10.1039/c1an15311k

32. Kodali DR, Small DM, Powell J, Krishnan K. Infrared Micro-imaging of Atherosclerotic Arteries. Appl Spectrosc. 1991;45: 1310–1317. doi:10.1366/0003702914335878

33. Wrobel TP, Majzner K, Baranska M. Protein profile in vascular wall of atherosclerotic mice analyzed ex vivo using FT-IR spectroscopy. Spectrochim Acta - Part A Mol Biomol Spectrosc. Elsevier B.V.; 2012;96: 940–945. doi:10.1016/j.saa.2012.07.103

34. Moreno PR. Detection of Lipid Pool, Thin Fibrous Cap, and Inflammatory Cells in Human Aortic Atherosclerotic Plaques by Near-Infrared Spectroscopy. Circulation. 2002;105: 923–927. doi:10.1161/hc0802.104291

35. Römer TJ, Brennan JF, Fitzmaurice M, Feldstein ML, Deinum G, Myles JL, et al. Histopathology of human coronary atherosclerosis by quantifying its chemical composition with Raman spectroscopy. Circulation. Am Heart Assoc; 1998;97: 878–885.

36. Wang L, Chapman J, Palmer R a., van Ramm O, Mizaikoff B. Classification of atherosclerotic rabbit aorta samples by mid-infrared spectroscopy using multivariate data analysis. J Biomed Opt. 2007;12: 024006. doi:10.1117/1.2714030

37. Toyran N, Severcan F, Severcan M, Turan B. Effects of selenium supplementation on rat heart apex and right ventricle myocardia by using FTIR spectroscopy: A cluster analysis and neural network approach. Food Chem. 2008;110: 590–597. doi:10.1016/j.foodchem.2008.02.044

38. Wald N, Legat A, Meyer C, Speiser DE, Goormaghtigh E. An infrared spectral signature of human lymphocyte subpopulations from peripheral blood. Analyst. Royal Society of Chemistry; 2015; doi:10.1039/c4an02247e

39. Krafft C, Salzer R, Soff G, Meyer-Hermann M. Identification of B and T cells in human spleen sections by infrared microspectroscopic imaging. Cytom Part A. 2005;64: 53–61. doi:10.1002/cyto.a.20117

40. Bassan P, Lee J, Sachdeva A, Pissardini J, Dorling KM, Fletcher JS, et al. The inherent problem of transflection-mode infrared spectroscopic microscopy and the ramifications

for biomedical single point and imaging applications. Analyst. 2013; 144–157. doi:10.1039/c2an36090j

41. Filik J, Frogley MD, Pijanka JK, Wehbe K, Cinque G. Electric field standing wave artefacts in FTIR micro-spectroscopy of biological materials. Analyst. 2012;137: 853. doi:10.1039/c2an15995c

42. Yeh K, Kenkel S, Liu J, Bhargava R. Fast Infrared Chemical Imaging with a Quantum Cascade Laser. Anal Chem. 2015;

43. Kole MR, Reddy RK, Schulmerich M V, Gelber MK, Bhargava R. Discrete frequency infrared microspectroscopy and imaging with a tunable quantum cascade laser. Anal Chem. 2012;84: 10366–72. doi:10.1021/ac302513f

44. Bhargava R, Fernandez DC, Hewitt SM, Levin IW. High throughput assessment of cells and tissues: Bayesian classification of spectral metrics from infrared vibrational spectroscopic imaging data. Biochim Biophys Acta. 2006;1758: 830–45. doi:10.1016/j.bbamem.2006.05.007

45. Jackson M, Choo LP, Watson PH, Halliday WC, Mantsch HH. Beware of connective tissue proteins: assignment and implications of collagen absorptions in infrared spectra of human tissues. Biochim Biophys Acta. 1995;1270: 1–6.

46. Fernandez DC, Bhargava R, Hewitt SM, Levin IW. Infrared spectroscopic imaging for histopathologic recognition. Nat Biotechnol. 2005;23: 469–74. doi:10.1038/nbt1080

47. Martin FL, Kelly JG, Llabjani V, Martin-Hirsch PL, Patel II, Trevisan J, et al. Distinguishing cell types or populations based on the computational analysis of their infrared spectra. Nat Protoc. 2010;5: 1748–1760. doi:10.1038/nprot.2010.133

48. Bhargava R. Towards a practical Fourier transform infrared chemical imaging protocol for cancer histopathology. Anal Bioanal Chem. 2007;389: 1155–69. doi:10.1007/s00216-007-1511-9

49. Pounder FN, Reddy RJ, Walsh MJ, Bhargava R. Validating the cancer diagnosis potential of mid-infrared spectroscopic imaging. Coté GL, editor. Proc SPIE. 2009;7186: 71860F–71860F–9. doi:10.1117/12.810122

50. Bhargava R, Levin IW. Fourier transform infrared imaging: theory and practice. Anal Chem. 2001;73: 5157–67.

51. Reddy RK, Bhargava R. Accurate histopathology from low signal-to-noise ratio spectroscopic imaging data. Analyst. 2010;135: 2818–25. doi:10.1039/c0an00350f

52. Wei L. Immunological aspect of cardiac remodeling: T lymphocyte subsets in inflammation-mediated cardiac fibrosis. Exp Mol Pathol. 2011;90: 74–8. doi:10.1016/j.yexmp.2010.10.004

53. Wang Q, Sanad W, Miller LM, Voigt A, Klingel K, Kandolf R, et al. Infrared imaging of compositional changes in inflammatory cardiomyopathy. Vib Spectrosc. 2005;38: 217–222. doi:10.1016/j.vibspec.2005.02.011

54. Fung MFK, Senterman MK, Mikhael NZ, Lacelle S, Wong PTT. Pressure-tuning Fourier Transform Infrared Spectroscopic Study of Carcinogenesis in Human Endometrium. Biospectroscopy. 1996;2: 155–165.

55. Sionkowska A, Wisniewski M, Skopinska J, Kennedy CJ, Wess TJ. Molecular interactions in collagen and chitosan blends. Biomaterials. 2004;25: 795–801. doi:10.1016/S0142-9612(03)00595-7

56. Parker FS. Applications of infrared spectroscopy in biochemistry , biology and medicine. 1971.

57. Burch GE, Sun S-C, Sohal RS, Chu K-C, Colcolough HL. Diphtheritic Myocarditis. Am J Cardiol. 1968;21: 261–268.

58. Hauck AJ, Kearney DL, Edwards WD. Evaluation of postmortem endomyocardial biopsy specimens from 38 patients with lymphocytic myocarditis: implications for role of sampling error. Mayo Clinic Proceedings. 1989. pp. 1235–1245.

59. Thomas Aretz H. Myocarditis: The Dallas criteria. Hum Pathol. W. B. Saunders Co.; 1987;18: 619–624. doi:10.1016/S0046-8177(87)80363-5

60. Wood BR, Quinn M a, Tait B, Ashdown M, Hislop T, Romeo M, et al. FTIR microspectroscopic study of cell types and potential confounding variables in screening for cervical malignancies. Biospectroscopy. 1998;4: 75–91. doi:10.1002/(SICI)1520-6343(1998)4:2<75::AID-BSPY1>3.0.CO;2-R

61. German MJ, Hammiche A, Ragavan N, Tobin MJ, Cooper LJ, Matanhelia SS, et al. Infrared Spectroscopy with Multivariate Analysis Potentially Facilitates the Segregation of Different Types of Prostate Cell. Biophys J. Elsevier; 2006;90: 3783–3795. doi:10.1529/biophysj.105.077255

62. Nasse MJ, Walsh MJ, Mattson EC, Reininger R, Kajdacsy-Balla A, Macias V, et al. High-resolution Fourier-transform infrared chemical imaging with multiple synchrotron beams. Nat Methods. 2011;8: 413–6. doi:10.1038/nmeth.1585

63. Walsh MJ, Mayerich D, Kajdacsy-Balla A, Bhargava R. High-resolution mid-infrared imaging for disease diagnosis. Mahadevan-Jansen A, Petrich W, editors. 2012;8219: 82190R. doi:10.1117/12.909339

64. Motz JT, Gandhi SJ, Scepanovic OR, Haka AS, Kramer JR, Dasari RR, et al. Real-time Raman system for in vivo disease diagnosis. J Biomed Opt. 2005;10: 031113. doi:10.1117/1.1920247

65. Motz JT, Fitzmaurice M, Miller A, Gandhi SJ, Haka AS, Galindo LH, et al. In vivo Raman spectral pathology of human atherosclerosis and vulnerable plaque. J Biomed Opt. 2006;11: 021003. doi:10.1117/1.2190967

66. Buschman HP, Marple ET, Wach ML, Bennett B, Schut TC, Bruining H a, et al. In vivo determination of the molecular composition of artery wall by intravascular Raman spectroscopy. Anal Chem. 2000;72: 3771–3775.

67. Mackanos M a., Contag CH. Fiber-optic probes enable cancer detection with FTIR spectroscopy. Trends Biotechnol. Elsevier Ltd; 2010;28: 317–323. doi:10.1016/j.tibtech.2010.04.001

68. Mackanos M a, Hargrove J, Wolters R, Du CB, Friedland S, Soetikno RM, et al. Use of an endoscope-compatible probe to detect colonic dysplasia with Fourier transform infrared spectroscopy. J Biomed Opt. 2014;14: 044006. doi:10.1117/1.3174387

69. Ferrari M, Mottola L, Quaresima V. Principles, techniques, and limitations of near infrared spectroscopy. Can J Appl Physiol. 2004;29: 463–487.

CHAPTER 2

Translation of Infrared Chemical Imaging for Cardiovascular Evaluation[2]

Abstract

Infrared (IR) spectroscopic imaging has been applied to study histology of cardiovascular tissue, primarily using Fourier transform IR (FTIR) Imaging. Here we describe results for histologic imaging of cardiac biopsies using a fast, discrete frequency IR (DFIR) imaging system. Histologic classification of tissue is understood in terms of the constituent frequencies and speeded up by careful optimization of the data acquired. Results are compared to FTIR imaging in terms of the signal to noise ratio and information content.

Introduction

Measuring local tissue morphology as well as expression of biochemical components such as collagen, glycogen, glycolipids is important for understanding and evaluating cardiovascular diseases. The typical assessment today focuses on assessing morphology and typically involves histological analysis and immunostaining that often provide qualitative data while requiring expensive reagents, time and effort of pathologist to determine the disease. Biochemical assays for molecular analyses of tissue are more quantitative in nature are but are usually destructive, often provide average values and do not allow for later use of tissue for other tests. Infrared spectrochemical imaging is a non-destructive tissue analysis method that can provide both qualitative and quantitative information, in an imaging format, about both the morphology and several biologically-important chemicals present. A major focus for IR imaging has been for developing protocols to analyze tissue.[1–6] Recent results have advanced the capabilities of IR

[2] Reprinted, with permission, from Saumya Tiwari, Jai Raman, Vijaya Reddy, Miranda Dawson, and Rohit Bhargava. "Translation of infrared chemical imaging for cardiovascular evaluation." In SPIE BiOS, pp. 97040X-97040X. International Society for Optics and Photonics, 2016. doi:10.1117/12.2230004

microscopes[7–9], computing[10] and theoretical understanding[11] as well as provided a number of interesting advances in high-definition spectral[12,13] and spectral-spatial methods[14,15] for tissue histology, cellular analysis[16–18], diagnosis of disease[19], obtaining prognostic information[20,21] and providing new visualizations for digital molecular pathology[22]. More recently, this technology has also garnered interest for identification of cardiovascular disorders[23–28].

In particular, previous studies using FTIR spectroscopy have identified bands with significant collagen contribution in order to study its distribution and remodeling in the cardiac tissue[29,30]. Rabee et al showed the correlation of band at 1338 cm^{-1} with immunohistochemical stain for collagen type I and trichrome stain[31]. This is important in identifying fibrosis[32,28], myocardial infarction[24,33], and specific type of collagen degradation can be related to cartilage degeneration[34]. Studying heart tissue can also give information about other diseases in body. For example, glycogen and glycolipid content is related to diabetes-related changes in heart[35] and chronic kidney disease can lead to accumulation of lipid in the cardiac tissue[36]. To study these diverse and varied effects, it is pertinent to not only develop infrared chemical imaging based detection models for heart tissue, but to also optimize speed of acquisition with data quality to enable extension of chemical imaging to other associated conditions. A major recent advance that promises high speed data acquisition and high-fidelity imaging lies in the development of IR spectral microscopes that employ quantum cascade lasers (QCL) as sources.[37–44] While several reports of these instruments exist, they haven't been used extensively for digital pathology yet and the area represents considerable potential for developing new protocols for clinical use. In this study, we discuss the translation of IR imaging for cardiovascular disease diagnostics using a discrete frequency IR (DFIR) instrument based on QCLs. In particular, we focus on demonstrating how a small number of spectral features[45] can rapidly provide diagnostically useful information.

Methods

Formalin-fixed, paraffin-embedded tissues were obtained from the archives of the department of Pathology, Rush University Medical center, Chicago. Samples were imaged using and FTIR

imaging spectrometer (Perkin Elmer Spotlight) and truncated to a range 748 cm^{-1} – 4000 cm^{-1} at spectral resolution of 8 cm^{-1} with step size of 4 cm^{-1} and square pixel size of 6.25 μm on each side. DFIR data was collected using Agilent Hyperscan system in the range 930 cm^{-1} to 1746 cm^{-1} using step size of 6 cm^{-1} and square pixel size of 5 μm on a side. ENVI IDL 4.8 (Environment for Visualizing Images with Interactive Data Language) software was used to process the image files. In order to eliminate non-cellular regions of the tissue sample, a mask was created that only selected a threshold of absorbance values at the amide I peak (1652 cm^{-1}). Specific regions of interest were applied to the same areas on both the DFIR and FTIR images. The average spectrum was then obtained at each of these regions. Resultant data was baseline corrected and normalized to the amide peak (1652 cm^{-1}). For unsupervised classification, iso data classification was used in ENVI IDL. Minimum number of classes was set at 4 while maximum number of classes was set at 5. A maximum of 3 iterations were performed with a change threshold of 10% with the condition that the classification would end before the set number of iterations if the number of pixels in each class changed by less than the threshold. In case of FTIR data, only spectral range of 900cm^{-1} to 1800cm^{-1} was used for classification. Finally, the relative intensities of collagen and glycogen were calculated with band math. Baseline corrected Amide III (1236 cm^{-1}) and glycogen (1032 cm^{-1}) absorbance values were divided by the values at the referential amide peak (1652 cm^{-1}). The resulting ratios were plotted in the form of color intensity map.

Results

Absorption spectra collected from same areas (normal myocardium) of two different samples collected on the FTIR instrument and DFIR system were compared, as shown in figure 1. The signal to noise ratio (SNR) obtained in case of hyperspectral scans of DFIR instrument was lower than the SNR obtained on FTIR instrument, while the peaks and peak widths in spectra were similar from both the instruments with some differences in the absorbance values. These differences are to be expected in terms of the different optics of the instrument and for different shapes within local sample morphology[46] and are relatively minor for most cases. We have also shown plotting of discrete frequencies with extrapolation for the same set of samples to

demonstrate the utilization of discrete frequency data to reproduce peaks of interest using a limited set of measurements, reducing scan time by manifolds.

An unsupervised Iso Data Classification algorithm was used to identify different classes present in the tissue. With the prior information that the sample had Myocardium, Fibrosis, Necrosis and non-tissue pixels, the minimum number of classes was set at 4. Myocardium regions, colored yellow in classified images, correlated with the Hematoxylin and Eosin (H&E) stain in both FTIR and DFIR data (Fig 2). Fibrosis and necrosis could not be differentiated from each other in terms of class label (green and blue colors). This was confirmed by plotting average spectra of the regions identified as Myocardium against other two classes (combined as "other"). In both the samples (Fig 3), regions other than myocardium showed higher intensity of normalized Amide III peak, indicating that these two classes had stronger contribution of collagen as compared to myocardium labelled class. This shows that both the data sets performed similar to each other in an unsupervised classification system. The extent of agreement in classification was not 100% and remains to be probed further.

While unsupervised classification gave a preliminary indication of applicability of DFIR data for identification of cell types, we further sought to examine if it could correlate with pathologist's observation of fibrosis, ischemia and amyloid deposition. Towards this end, we plotted the relative band intensities of the Amide III and the glycogen-specific features which contributed at band 1032cm^{-1} with Amide I band (Fig 4). As expected, collagen expression, which is a major contributor to Amide III correlated highly with pathologist identified regions of fibrosis as noted in our earlier studies[47]. We expected to see variations in levels of glycogen for samples with ischemia, but notable differences were not found in these samples compared to control healthy samples. This could be possibly due to glycogen washing out during sample preparation steps, but further studies would be needed to provide a definitive answer. Interestingly, peak height ratio of 1032cm^{-1} band with Amide I band appeared significantly high in samples reported to have amyloid deposition (Fig 4, last panel). This is an exciting discovery since it is very difficult to distinguish between amyloid depositions and fibrosis through H&E stains alone. As expected, this could not be differentiated directly via the Amide III band intensity color map since both collagen and amyloid deposits contribute overlapping vibrational modes within the band.

Introduction of DFIR systems to routine lab use and data analysis towards pathology has shown very promising outcomes. Our results indicate that not only can DFIR data be applied in a similar manner as FTIR data towards digital pathology, it also has potential to enable pathologists identify regions that are visibly similar but biochemically different in their traditional staining methods. The findings reported here are on a small data set and would need further validation on larger data sets. A detailed protocol will need to be constructed and statistical validation understood in light of various other factors[48] before attempts at clinical translation. At present, this works demonstrated the potential of DFIR imaging and its excellent capacity towards digital pathology for cardiovascular diseases.

Conclusion

In this paper, we describe the application of a DFIR imaging system for the analysis of cardiovascular biopsy samples. Although much work needs to be done in order to make the SNR comparable to conventional FTIR imaging systems and the development of a clinically translatable protocol, it can be seen that the technology performs well in identification of many biochemical signals. This approach can be a nice complement to other emerging approaches for intraoperative aseessment[34].

Acknowledgement

This study was partially supported by funding from the National Institutes of Health via grant number R01 GM117594. The authors would also like to acknowledge Andrew Ghetler, Richard P. Tella, Yang Han, Christopher R. Moon and Charles D. Hoke from California Research Center, Spectroscopy & Vacuum Solutions Division, Agilent Technologies, Inc. and Agilent Technologies Inc. for providing the DFIR instrument used in this study.

Figures

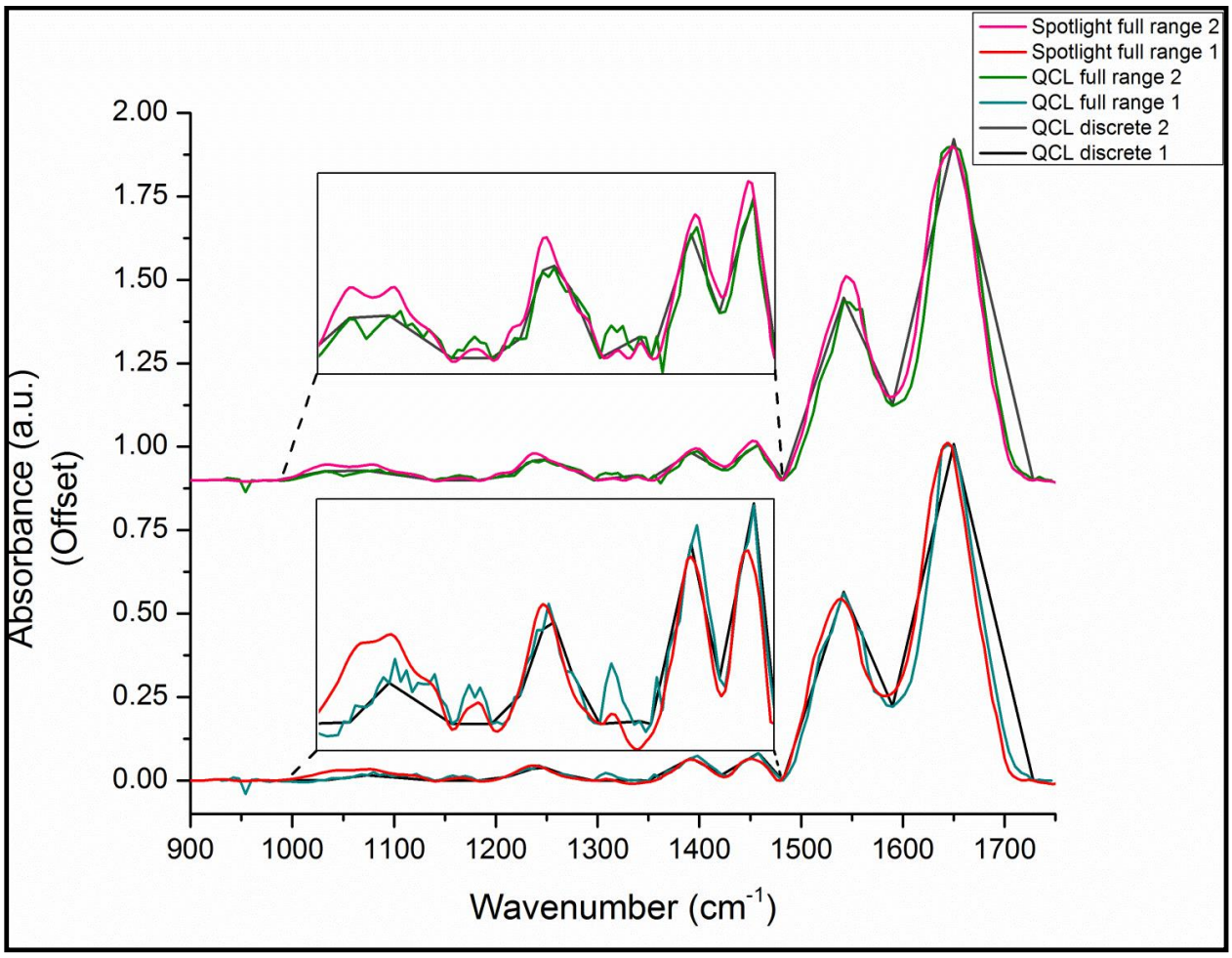

Figure 7: Absorption spectra of two cardiac biopsy samples collected on Fourier transform infrared (FTIR) spectroscopic imaging and quantum cascade laser (QCL)-based discrete frequency instrument.

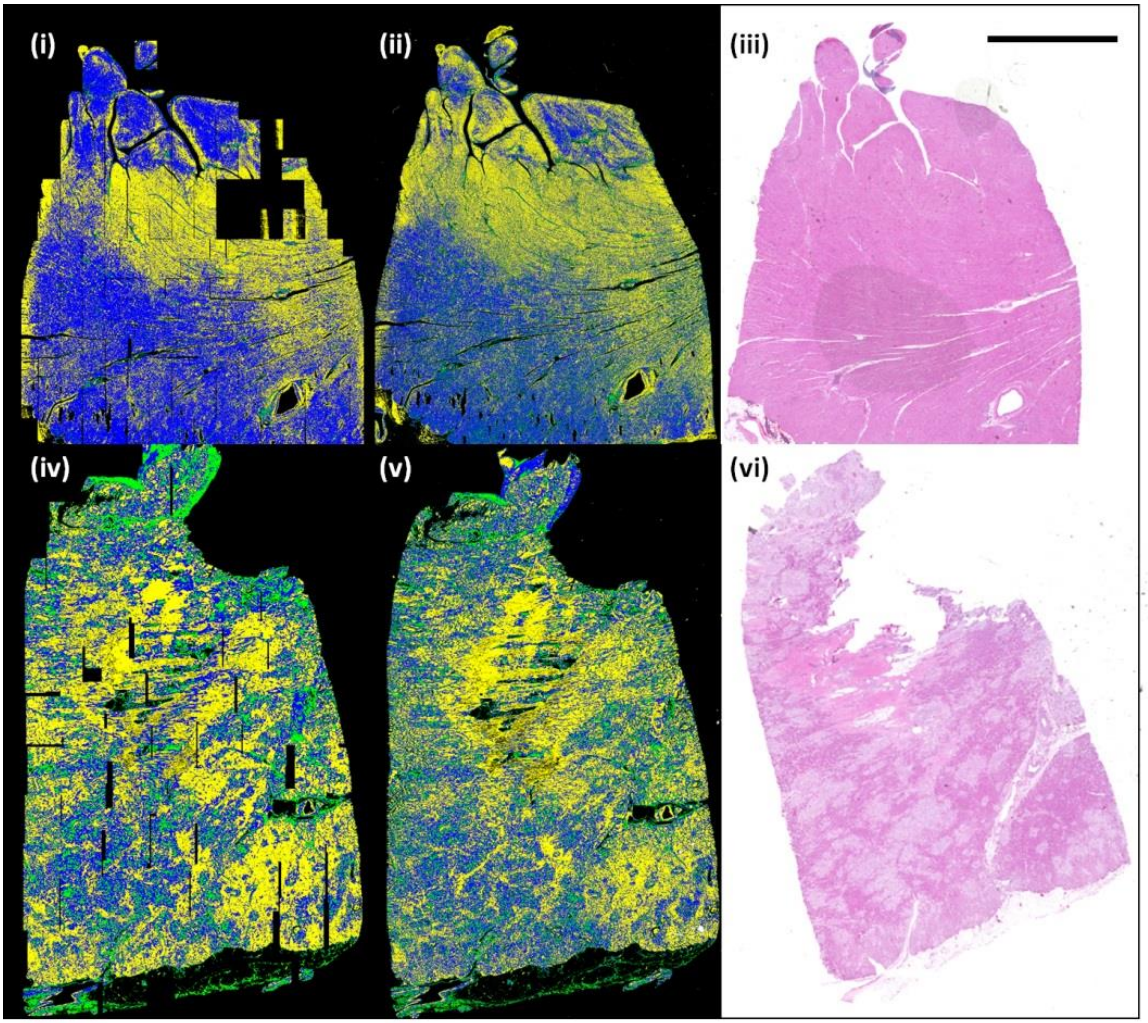

Figure 8: Iso Data unsupervised classification on FTIR ((i) and (iv)) and DFIR ((ii) and (v)) data. Scale bar on H&E image indicates 6 mm.

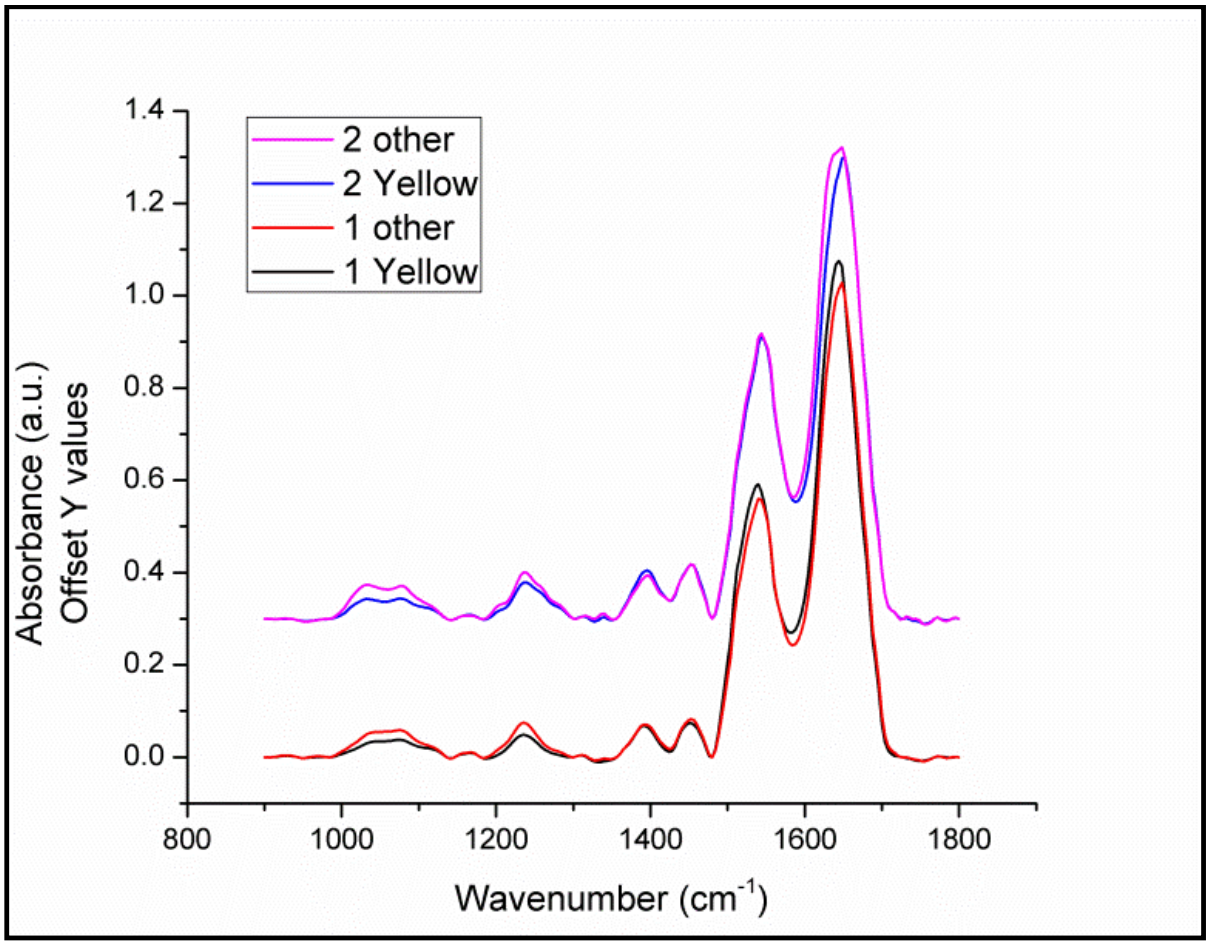

Figure 9: Spectral comparison of classes obtained using unsupervised classification. Data shown is from FTIR instrument corresponding to classes identified in figure 2.

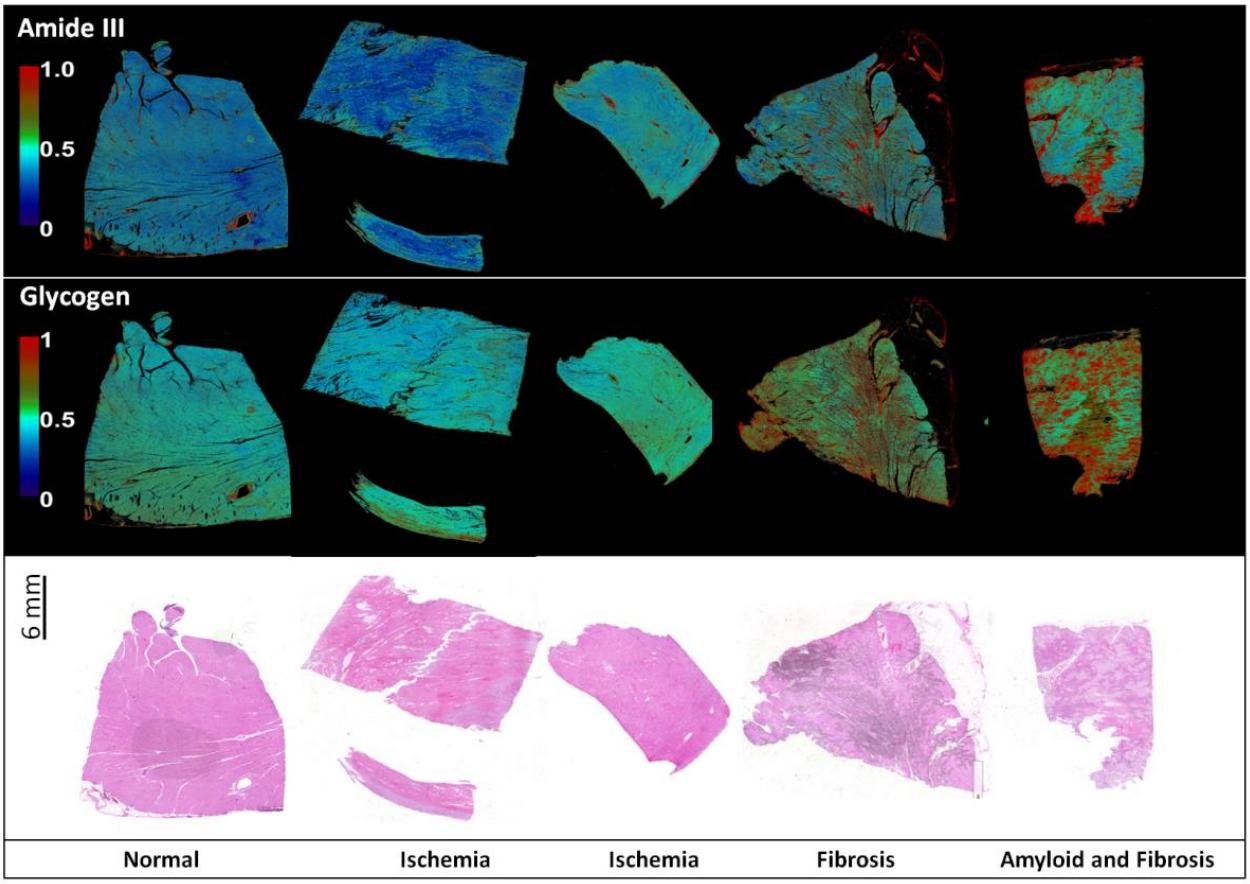

Figure 10: Absorbance of Amide III at 1236cm^{-1} (top) and Glycogen at 1032 cm^{-1} (middle) normalized by ratio with Amide I peak obtained from DFIR imaging data show good correspondence with macroscopic structure seen in conventional H&E stained histologic images (bottom).

References

1. Fernandez DC, Bhargava R, Hewitt SM, Levin IW. Infrared spectroscopic imaging for histopathologic recognition. Nat. Biotechnol. 2005;23(4):469-74. doi:10.1038/nbt1080.

2. Conti C, Ferraris P, Giorgini E, et al. FT-IR microimaging spectroscopy: A comparison between healthy and neoplastic human colon tissues. J. Mol. Struct. 2008;881(1-3):46-51. doi:10.1016/j.molstruc.2007.08.040.

3. Bird B, Miljković MS, Remiszewski S, Akalin A, Kon M, Diem M. Infrared spectral histopathology (SHP): a novel diagnostic tool for the accurate classification of lung cancer. Lab. Invest. 2012;92(9):1358-73. doi:10.1038/labinvest.2012.101.

4. Diem M, Mazur A, Lenau K, et al. Molecular pathology via IR and Raman spectral imaging. J. Biophotonics 2013;6(11-12):855-86. doi:10.1002/jbio.201300131.

5. Bhargava R. Towards a practical Fourier transform infrared chemical imaging protocol for cancer histopathology. Anal. Bioanal. Chem. 2007;389(4):1155-69. doi:10.1007/s00216-007-1511-9.

6. Tiwari S, Bhargava R. Extracting knowledge from chemical imaging data using computational algorithms for digital cancer diagnosis. Yale J. Biol. Med. 2015;88(2):131-43.

7. Nasse MJ, Walsh MJ, Mattson EC, et al. High-resolution Fourier-transform infrared chemical imaging with multiple synchrotron beams. Nat. Methods 2011;8(5):413-6. doi:10.1038/nmeth.1585.

8. Walsh MJ, Mayerich D, Kajdacsy-Balla A, Bhargava R. High-resolution mid-infrared imaging for disease diagnosis. Mahadevan-Jansen A, Petrich W, eds. 2012;8219:82190R. doi:10.1117/12.909339.

9. Mayerich D, van Dijk T, Walsh MJ, Schulmerich M V, Carney PS, Bhargava R. On the

importance of image formation optics in the design of infrared spectroscopic imaging systems. Analyst 2014;139(16):4031-6. doi:10.1039/c3an01687k.

10. Mayerich D, Walsh M, Schulmerich M, Bhargava R. Real-time interactive data mining for chemical imaging information: application to automated histopathology. BMC Bioinformatics 2013;14:156. doi:10.1186/1471-2105-14-156.

11. Reddy RK, Walsh MJ, Schulmerich M V, Carney PS, Bhargava R. High-definition infrared spectroscopic imaging. Appl. Spectrosc. 2013;67(1):93-105. doi:10.1366/11-06568.

12. Leslie LS, Wrobel TP, Mayerich D, Bindra S, Emmadi R, Bhargava R. High definition infrared spectroscopic imaging for lymph node histopathology. PLoS One 2015;10(6):e0127238. doi:10.1371/journal.pone.0127238.

13. Nallala J, Lloyd GR, Shepherd N, Stone N. High-resolution FTIR imaging of colon tissues for elucidation of individual cellular and histopathological features. Analyst 2016;141(2):630-9. doi:10.1039/c5an01871d.

14. Sreedhar H, Varma VK, Nguyen PL, et al. High-definition Fourier Transform Infrared (FT-IR) spectroscopic imaging of human tissue sections towards improving pathology. J. Vis. Exp. 2015;(95):52332. doi:10.3791/52332.

15. Pounder FN, Reddy RK, Bhargava R. FDVIBSPC16: Development of a practical spatial-spectral analysis protocol for breast histopathology using Fourier transform infrared spectroscopic imaging. Faraday Discuss. 2016. doi:10.1039/C5FD00199D.

16. Holton SE, Bergamaschi A, Katzenellenbogen BS, Bhargava R. Integration of molecular profiling and chemical imaging to elucidate fibroblast-microenvironment impact on cancer cell phenotype and endocrine resistance in breast cancer. PLoS One 2014;9(5):e96878. doi:10.1371/journal.pone.0096878.

17. Smolina M, Goormaghtigh E. Infrared imaging of MDA-MB-231 breast cancer cell line phenotypes in 2D and 3D cultures. Analyst 2015;140(7):2336-43.

doi:10.1039/c4an01833h.

18. Tiwari S, Zong X, Holton SE, Prasanth K V., Bhargava R. Fourier transform infrared (FT-IR) spectroscopy and imaging of the nucleus to characterize DNA contributions in different phases of the cell cycle. In: Gimi B, Molthen RC, eds. SPIE Medical Imaging. International Society for Optics and Photonics; 2015:941720. doi:10.1117/12.2082347.

19. Großerueschkamp F, Kallenbach-Thieltges A, Behrens T, et al. Marker-free automated histopathological annotation of lung tumour subtypes by FTIR imaging. Analyst 2015;140(7):2114-20. doi:10.1039/c4an01978d.

20. Kwak JT, Kajdacsy-Balla A, Macias V, Walsh M, Sinha S, Bhargava R. Improving Prediction of Prostate Cancer Recurrence using Chemical Imaging. Sci. Rep. 2015;5:8758. doi:10.1038/srep08758.

21. Hughes C, Baker MJ. Can mid-infrared biomedical spectroscopy of cells, fluids and tissue aid improvements in cancer survival? A patient paradigm. Analyst 2016;141(2):467-75. doi:10.1039/c5an01858g.

22. Mayerich D, Walsh MJ, Kadjacsy-Balla A, Ray PS, Hewitt SM, Bhargava R. Stain-less staining for computed histopathology. TECHNOLOGY 2015:1-5. doi:10.1142/S2339547815200010.

23. P. Wrobel T, Mateuszuk L, Chlopicki S, Malek K, Baranska M. Imaging of lipids in atherosclerotic lesion in aorta from ApoE/LDLR−/− mice by FT-IR spectroscopy and Hierarchical Cluster Analysis. Analyst 2011;136:5247. doi:10.1039/c1an15311k.

24. Yang TT, Weng SF, Zheng N, et al. Histopathology mapping of biochemical changes in myocardial infarction by Fourier transform infrared spectral imaging. Forensic Sci. Int. 2011;207(1-3):e34-9. doi:10.1016/j.forsciint.2010.12.005.

25. Colley CS, Kazarian SG, Weinberg PD, Lever MJ. Spectroscopic imaging of arteries and atherosclerotic plaques. Biopolymers 2004;74(4):328-35. doi:10.1002/bip.20069.

26. Palombo F, Shen H, Benguigui LES, Kazarian SG, Upmacis RK. Micro ATR-FTIR spectroscopic imaging of atherosclerosis: an investigation of the contribution of inducible nitric oxide synthase to lesion composition in ApoE-null mice. Analyst 2009;134(6):1107-18. doi:10.1039/b821425e.

27. Bonnier F, Bertrand D, Rubin S, et al. Detection of pathological aortic tissues by infrared multispectral imaging and chemometrics. Analyst 2008;133(6):784-90. doi:10.1039/b717164a.

28. Tiwari S, Reddy VB, Bhargava R, Raman J. Computational chemical imaging for cardiovascular pathology: chemical microscopic imaging accurately determines cardiac transplant rejection. PLoS One 2015;10(5):e0125183. doi:10.1371/journal.pone.0125183.

29. Liu K-Z, Dixon IMC, Mantsch HH. Distribution of Collagen Deposition in Cardiomyopathic Hamster Hearts Determined by Infrared Microscopy. Cardiovasc. Pathol. 1999;8(1):41-47. doi:10.1016/S1054-8807(98)00024-6.

30. Gough KM, Zelinski D, Wiens R, Rak M, Dixon IMC. Fourier transform infrared evaluation of microscopic scarring in the cardiomyopathic heart: Effect of chronic AT1 suppression. Anal. Biochem. 2003;316(2):232-242. doi:10.1016/S0003-2697(03)00039-3.

31. Cheheltani R, Rosano JM, Wang B, Sabri AK, Pleshko N, Kiani MF. Fourier transform infrared spectroscopic imaging of cardiac tissue to detect collagen deposition after myocardial infarction. J. Biomed. Opt. 2012;17(5):56014. doi:10.1117/1.JBO.17.5.056014.

32. Bromberg PS, Gough KM, Dixon IM. Collagen remodeling in the extracellular matrix of the cardiomyopathic Syrian hamster heart as assessed by FTIR attenuated total reflectance spectroscopy. Can. J. Chem. 2011.

33. Lui K, Jackson M, Sowa MG, Ju H, Dixon IM, Mantsch HH. Modification of the

extracellular matrix following myocardial infarction monitored by FTIR spectroscopy. Biochim. Biophys. Acta 1996;1315(2):73-7.

34. West P a., Bostrom MPG, Torzilli P a., Camacho NP. Fourier transform infrared spectral analysis of degenerative cartilage: An infrared fiber optic probe and imaging study. Appl. Spectrosc. 2004;58(4):376-381. doi:10.1366/000370204773580194.

35. Toyran N, Lasch P, Naumann D, Turan B, Severcan F. Early alterations in myocardia and vessels of the diabetic rat heart: an FTIR microspectroscopic study. Biochem. J. 2006;397:427-436. doi:10.1042/BJ20060171.

36. Kuwahara M, Bannai K, Segawa H, Miyamoto K, Yamato H. Cardiac remodeling associated with protein increase and lipid accumulation in early-stage chronic kidney disease in rats. Biochim. Biophys. Acta 2014;1842(9):1433-43. doi:10.1016/j.bbadis.2014.04.026.

37. Yeh K, Kenkel S, Liu J, Bhargava R. Fast Infrared Chemical Imaging with a Quantum Cascade Laser. Anal. Chem. 2015.

38. Kröger N, Egl A, Engel M, et al. Quantum cascade laser-based hyperspectral imaging of biological tissue. J. Biomed. Opt. 2014;19(11):111607. doi:10.1117/1.JBO.19.11.111607.

39. Bassan P, Weida MJ, Rowlette J, Gardner P. Large scale infrared imaging of tissue micro arrays (TMAs) using a tunable Quantum Cascade Laser (QCL) based microscope. Analyst 2014;139(16):3856-9. doi:10.1039/c4an00638k.

40. Kole MR, Reddy RK, Schulmerich M V, Gelber MK, Bhargava R. Discrete frequency infrared microspectroscopy and imaging with a tunable quantum cascade laser. Anal. Chem. 2012;84(23):10366-72. doi:10.1021/ac302513f.

41. Phillips MC, Ho N. Infrared hyperspectral imaging using a broadly tunable external cavity quantum cascade laser and microbolometer focal plane array. Opt. Express 2008;16(3):1836. doi:10.1364/OE.16.001836.

42. Guo B, Wang Y, Peng C, Luo GP, Le HQ. Multi-Wavelength Mid-Infrared Micro-Spectral Imaging using Semiconductor Lasers. Appl. Spectrosc. 2003;57(7):811-822. doi:10.1366/000370203322102906.

43. Haase K, Kröger-Lui N, Pucci A, Schönhals A, Petrich W. Real-time mid-infrared imaging of living microorganisms. J. Biophotonics 2016;9(1-2):61-6. doi:10.1002/jbio.201500264.

44. Kröger-Lui N, Gretz N, Haase K, et al. Rapid identification of goblet cells in unstained colon thin sections by means of quantum cascade laser-based infrared microspectroscopy. Analyst 2015;140(7):2086-92. doi:10.1039/c4an02001d.

45. Bhargava R, Fernandez DC, Hewitt SM, Levin IW. High throughput assessment of cells and tissues: Bayesian classification of spectral metrics from infrared vibrational spectroscopic imaging data. Biochim. Biophys. Acta 2006;1758(7):830-45. doi:10.1016/j.bbamem.2006.05.007.

46. van Dijk T, Mayerich D, Carney PS, Bhargava R. Recovery of absorption spectra from Fourier transform infrared (FT-IR) microspectroscopic measurements of intact spheres. Appl. Spectrosc. 2013;67(5):546-52. doi:10.1366/12-06847.

47. Tiwari S, Raman J, Reddy V, et al. Translating infrared spectroscopic imaging for rapid analysis of clinical biopsy samples using a discrete frequency approach.

48. Kwak JT, Reddy R, Sinha S, Bhargava R. Analysis of variance in spectroscopic imaging data from human tissues. Anal. Chem. 2012;84(2):1063-9. doi:10.1021/ac2026496.

CHAPTER 3

Towards Translation of Discrete Frequency Infrared Imaging for Rapid Digital Histopathology of Clinical Biopsy Samples[3]

Abstract

Fourier transform infrared (FT-IR) spectroscopic imaging has been widely tested as a tool for stainless digital histology of biomedical specimens, including for identification of infiltration and fibrosis in endomyocardial biopsy samples to assess transplant rejection. A major barrier in clinical translation has been the slow speed of imaging. To address this need, we tested and report here the viability of using high speed discrete frequency infrared (DFIR) imaging to obtain stain-free biochemical imaging in cardiovascular samples collected from patients. Images obtained by this method were classified with high accuracy by a Bayesian classification algorithm trained on FT-IR imaging data as well as on DFIR data. A single spectral feature correlated with instances of fibrosis, as identified by the pathologist, highlighting the advantage of the DFIR imaging approach for rapid detection. The speed of digital pathologic recognition was at least 16 times faster than the fastest FT-IR imaging instrument. These results indicate that a fast, on-site identification of fibrosis using IR imaging has potential for real time assistance during surgeries. Further, the work describes development and applications of supervised classifiers on DFIR imaging data, comparing classifiers developed on FT-IR and DFIR imaging modalities and identifying specific spectral features for accurate identification of fibrosis. This addresses a topic of much debate on the use of training data and cross-modality validity of IR measurements. Together, the work is a step towards addressing a clinical diagnostic need at acquisition time scales that make IR imaging technology practical for medical use.

Introduction

[3] Reprinted, with permission, from Saumya Tiwari, Jai Raman, Vijaya Reddy, Andrew Ghetler, Richard P Tella, Yang Han, Christopher R Moon, Charles D Hoke, Rohit Bhargava. "Towards Translation of Discrete Frequency Infrared Spectroscopic Imaging for Digital Histopathology of Clinical Biopsy Samples." Analytical Chemistry 88.20 (2016): 10183-10190. doi: 10.1021/acs.analchem.6b02754

Cardiovascular diseases (CVDs) are the leading cause of mortality in the United States, accounting for one in seven deaths1. Histopathological examination is often the final arbiter in making diagnoses and guiding therapy for a variety of CVDs, largely relying on manual examination of microscopic structures in tissue that become apparent only by the application of exogenous contrast agents such as dyes and fluorescent probes. As opposed to cancer pathology, in which gross tissue changes allow a simple recognition of disease in most cases, tissue changes are more subtle in CVDs and require careful human examination. Due to the need for tissue processing and staining followed by manual examination, the recognition process cannot be real-time. Consequently, there remains a large temporal gap between histopathological analyses in the laboratory and the need for input in the surgical suite. A number of stainless staining and diagnosis approaches have been suggested to visualize tissue structure2, including those focused on CVDs3. While these technologies have shown promise in performing histologic analyses, the data acquisition has been slow and incapable of addressing the time gap to bring real-time pathology to the site of intervention where it can have the most impact.

Fourier transform infrared (FT-IR) spectroscopic imaging has shown great promise in cellular recognition4–8, metabolic analysis9,10, disease diagnoses11,12 and prognosis13,14. In FT-IR imaging, approximately 2000 spectral elements are typically acquired per pixel in the image. Using a metrics based approach15,16, it has long been demonstrated that not all recorded data may be needed for accurate histologic recognition. By using Bayesian classification, for example, a subset of data can be identified that gives accurate classification15 using 10-50 metrics for many different types of tissues15. Hence, the potential exists to decrease time for providing histologic images from a sample simply by acquiring only the needed data and increasing analysis speed ~20-100-fold. This concept, however, has not been previously realized. With the development of discrete frequency IR imaging instruments17,18 single band images can be generated within seconds for areas of the order of cm2 and pixel size of the order of microns. While initial attempts using filters19 did not provide high signal to noise ratio (SNR) for practical use, quantum cascade laser (QCL)-based microscopes20–23 have dramatically improved and shown promise for tissue imaging24,25. In a previous study, we used unsupervised clustering to differentiate between biochemically different regions in cardiac biopsy samples26. Recently, a

two class classifier was used to differentiate between cancerous and normal epithelium using DFIR imaging25. Since the technology is relatively new, a number of issues remain to be resolved. First, it is not clear whether spectral features for DFIR imaging should or can be selected from FT-IR imaging data, which provides access to all the possible spectral features and high SNR. Or alternately, it is not known whether classification should be developed de novo using DF data that suffers from low SNR but would remove imaging modality dependent effects. Second, the advantage of the DF approach is not apparent. In order to utilize the speed advantage of the system, an ideal case scenario would be a single spectral feature to differentiate between the classes but it is unclear whether the SNR of the data are sufficient to permit such a determination. Finally, multiclass classifiers have not been developed on DFIR imaging data. This raises questions about the possibility and accuracy in identifying multiple classes with DF technology. In this study, we focus on these extant issues. Specifically, we demonstrate the application of DFIR imaging for automated pathology of CVDs by analyzing the performance of different two-class and multiclass classifiers and its potential for clinical implementation. Optimizing recognition, we also show that a single spectral feature was sufficient to differentiate between two histopathological classes, namely myocardium and fibrosis, giving tremendous advantage in terms of speed of detection. Finally, we sought to demonstrate rapid digital pathology for use in evaluating cardiac tissue, since intra-operative recognition can be advantageous in real-time.

Methods:

Sample acquisition

Fourteen patient samples were collected in collaboration with Rush University Medical Center. All sections provided were anonymized and no patient identifying information was recorded for the experiments. The samples were formalin fixed, paraffin embedded and microtomed onto low E glass slides (Kevley Technologies) at 5μm slice thickness for infrared imaging. Deparaffinization was performed by repeated hexane washes for 24 hours before imaging. No further processing was required for the samples for IR imaging. A serial section was acquired on a glass slide for each sample to perform Hematoxylin and Eosin (H&E) stain. An expert pathologist identified histologically relevant regions in the biopsies. Based on this, 10 patient samples were identified to have histologically normal myocardium regions and seven samples contained regions identified as fibrosis. In addition, previously collected thirty-five anonymized patient samples' FT-IR imaging data were used to develop the FT-IR imaging data-based classifiers.

Data acquisition and processing

FT-IR imaging data were acquired using a 4 cm-1 spectral resolution, a 6.25 micron pixel size and one scan per pixel following sample preparation and image collection protocols described earlier27–29. For each image, a background was collected using identical spectral and spatial parameters with 120 spectral co-additions. DFIR data was acquired on Agilent LaserDirect IR imaging system using a reflection-absorption sampling geometry. The instrument settings allowed data collection at 1, 3, 5 and 10 □m pixel sizes and pixel size of 5 □m was chosen for imaging. When acquiring spectra, a step size of 6 cm-1 was used to step the discrete frequencies of the quantum cascade laser source. DFIR data were imported using MATLAB and further processing was performed in Environment for Visualization (ENVI) - Interactive Data Language (IDL) version 4.8. Programs for Bayesian classification were developed in-house and implemented in ENVI. The data collected in the form of tiles was mosaicked in ENVI-IDL using in house written algorithms. Tissue pixels were selected by creating a mask at threshold value of

0.2 of peak height at 1652 cm-1 after a linear baseline correction using absorbance values at 1482 cm-1 and 1710 cm-1.

Development of FT-IR classifier

In a previous study, we had developed a Bayesian classifier to identify myocardium, fibrosis and lymphocytic infiltration3 following earlier protocols15,29. Briefly, the data was converted into quantitative ratios of spectral features or characteristics of individual bands called metrics. This was done by specifying 148 spectral features which corresponded to peak height ratios, peak area to height ratios, peak area to area ratios and centroid position of peaks for every pixel. The ground truth was specified by marking regions of interest (ROI) on IR images corresponding to pathologist annotated regions on the H&E image from a serial section. These metrics and associated ground truth marked pixels were used to train the classifier. We did not use the previously built FT-IR imaging data based Bayesian classifier as-is since the range of the DF instrument is 800 cm-1 to 1900 cm-1, whereas the original FT-IR imaging data based classifier utilized the range of 750 cm-1 to 4000 cm-1. A new Bayesian classifier was developed using the truncated FT-IR imaging data and validated on independent set of FT-IR imaging data before applying it to DF-IR imaging data. Receiver Operating Characteristic (ROC) curves were calculated for FT-IR imaging data training and validation sets. All images acquired in DF-IR imaging mode were classified with this classifier and ROC curves, confusion matrix and overall accuracy were calculated for DF-IR images with previously established ground truth in ENVI-IDL.

Development of DF-IR classifier

Data preprocessing was performed as described in section 2.2. Data to metric conversion was performed by defining 185 metrics in the DFIR data based on spectral variations observed in the data. In order to develop Bayesian classifier, the DF-IR data was split into training and validation set. Seven samples were used for training the classifier. In case of multi-class classifier, for each of the training and validation sets, at least three patient samples were marked with myocardium, fibrosis and blood class. One additional ‘cell death’ class was added through one sample in training and two samples in validation. Ground truth was marked on this data using pathologist

annotated H&E images. Only the regions with high confidence in identifying histological classes were marked. Bayesian classifier was developed on this data set using previously developed protocols. ROC curves were calculated for both training and validation datasets. Confusion matrix and overall accuracy was calculated on classified image acquired from validation set. Both confusion matrix and ROC curves were calculated in ENVI IDL prebuilt toolbox for post-classification processing.

Specific band based detection

Spectral features which led to correct classification in the classifier models were considered individually to identify features that offered high overall accuracy of distinguishing between myocardium and fibrosis. In order to distinguish between the classes, a threshold was used to separate the two classes from each other. Multiple thresholds were tested on each band individually for overall accuracy in separation of classes and the spectral feature with highest overall accuracy was chosen. Class images were created at the threshold which produced highest accuracy and confusion matrix was calculated using the previously established ground truth.

Results and Discussion

Data collection and analysis on DFIR imaging instrument

We imaged identical areas of two patient samples using both FT-IR and DFIR systems to compare the spatial and spectral features of data acquired using the two different modalities. Images of the Amide I absorbance were used to compare spatial quality and fidelity. No other corrections were performed on the images (figure 1 (A, B, E, F)). Comparing spectra obtained from FT-IR and DFIR systems using the same area in tissue and background, it can be observed that the raw spectra averaged over >5000 pixels have similar spectral characteristics in terms of peak positions (figure 1 (C, G)). While averaging provided similar quality spectra, point-by-point comparisons of spectra showed some differences likely arising from differences in optical configuration30 and noise. In addition to small differences in absorption, DFIR spectra had lower SNR (figure 1 (D, H)). As opposed to FT-IR imaging data that have uniform noise across the spectrum due to the transformation from the retardation to the spectral domain, the DFIR

instrument reflected the underlying fluctuations at specific positions even apparent in single beam background spectra. This not only makes the noise non-uniform across the spectrum (figure 1 (C, G)) but is likely correlated with laser intensity fluctuations as well making, as common for shot noise in most lasers, it difficult to signal average.

A major factor in successful classification is the quality of the data, which typically implies an increase in measurement time per pixel or decrease in total area covered, to increase the SNR. To determine the speed advantage of DFIR instrument, we first acquired data at the maximum rate of approximately 15 seconds per band at 5 μm pixel size, which is the typical cellular size, and for a sample area of ~2 mm x 2 mm, which is the typical biopsy size. It is difficult to achieve a straightforward comparison of this scan time with an FT-IR imaging system, since the techniques are fundamentally different in light utilization, spectral bandwidth and modulation. A general comparison of QCL and FT-IR imaging is available18 by normalizing the performance of instruments by considering number of pixels imaged, SNR and the time required for image collection. A similar examination can be conducted for point microscopy systems with this system17, but is not productive. FT-IR point microscopy systems do not typically perform well at low aperture settings and need a synchrotron31 for these aperture sizes. A more reasonable comparison is between a globar-equipped FT-IR imaging system without apertures and the DFIR approach with this bright light source. Each system is playing to its advantages in such a comparison, i.e. the light of the large sized globar source is used for widefield imaging while the collimated and narrow laser light is used for point microscopy. In this task-based comparison of fit for purpose instruments, we proposed that the time required by the DFIR imaging approach be compared to the FT-IR imaging approach to obtain a spectral classification. We focused on getting the highest possible SNR that could be obtained from the DFIR instrument. In figure 2, the effects of signal averaging are demonstrated for low and high speed settings, which corresponded to a higher and lower detector integration time respectively. Figure 2(A) compares the size of the images at various resolution settings, showing no appreciable change in features. The SNR did not change significantly by changing speed as seen from the spectral profile of 5 x 5 block of pixels in figure 2(B). This is understandable since, as opposed to FT-IR imaging systems, the SNR is dominated by laser fluctuations and not by detector noise. Since our goal

was to reduce the imaging time, high speed settings were used henceforth. Next, we compared the time required to collect images at different pixel sizes for the full range provided by the instrument (figure 2(C)) for an area of 2.5 mm2. For comparison, the same area was imaged using an FT-IR imaging system with typical parameters for spatial and spectral resolution. A comparable spectral range could be obtained by using an undersampling ratio to reduce the FT-IR scan time further by more than a factor of 2.

For images taken over the full spectral range of the DFIR instrument and pixel sizes of 5-10 μm, the system does not offer significant speed advantages compared to the FT-IR approach. The higher intensity of the QCL is an advantage but the low noise thermal source, and the efficient interferometry process proves remarkably competitive. However, for the acquisition of a small number of bands, the time taken by the DFIR system reduces proportionally. Therefore, even though the initial research time required for developing classification algorithms would still remain comparable to FT-IR imaging systems due to the need for acquiring spectra over the entire bandpass, it is only the combination of DFIR acquisition with metrics-based classification that can enable rapid diagnoses in routine application to samples. The caveat here is the difference in SNR obtained from the two instruments, which is known to affect the classification accuracy32. While commercial FT-IR imaging instruments offer a spectral SNR of above 200, the DFIR instrument used in this study had at least 5 times lower SNR. Thus, two important future improvements are apparent. First, SNR can be improved by improving the hardware and image collection protocols. Second, post-acquisition noise reduction techniques need to be developed for discrete frequency data32; in order to be not limited by SNR for obtaining high classification accuracy. While the former is likely to be a major focus for the field in the coming years, the latter offers a solution that can be implemented faster.

Classifier training on FT-IR data and application on discrete frequency data

The underlying assumption in development of spectral Bayesian classification protocols is that switching between image collection modalities would not affect the results in identification of cell types since inherent biochemical contrast is utilized for chemical staining. To test this assumption, we first trained a Bayesian classifier on FT-IR imaging data to identify histologically normal myocardium and fibrotic regions. Upon calibrating in 900-1800 cm-1 range, 13 metrics were identified to provide adequate performance (Supplementary table 1). The classifier generated from this data, in the form of probability distribution functions and list of metrics to use for classification was applied as-is to DFIR data. ROC curves generated for this classifier are shown in figure 3 ((i), (ii) and (iii)); along with the representative classified images and their comparison with H&E stained images (figure 4 (A, E, I)). The regions identified by the pathologist as fibrosis have been marked with arrow in figure 4 (D, H, L). Correspondingly, fibrotic regions can be seen in classified IR image. When a control sample with no fibrosis (figure 4 (A)) was classified, we did not observe any bulk fibrosis in the classification. Comparing the ROC curves obtained by applying the classifier on FT-IR and DFIR data, it is clear that the classifier had lower area under the ROC curve for DF-IR data. The overall accuracy of classification was calculated to be 94.42% (Table 1) on the DFIR dataset that was also used for validation in section 3.3 in order to remove effect of marking ground truth while comparing performance of FT-IR and DFIR classifier. In conclusion, DFIR data could be classified with high correspondence to pathologist identified classes using classifier developed on FT-IR data, though not perfectly, with overall accuracy in the neighborhood of 95%.

Development of classifiers on DFIR data

In order to understand whether high sensitivity and specificity classifiers can be built on DF data due to its noise characteristics, we started with a binary classification model with myocardium and fibrosis classes. The training and validation sets were split and classified as described in methods. Using the Baysian approach, 11 metrics were identified which contributed in the decision making of the classifier (Supplementary table 2). We calculated the ROC curves of training and validation data sets (Figure 3 (iv) and (v)) and observed that the area under the curves (AUC) of the ROC of classifier trained on DFIR data was lower as compared to the classifier trained on FT-IR data. The accuracy was 90.99% (Table 2). Figure 4 (B, F, J) shows a comparison of images identified with this classifier with corresponding H&E images in Figure 4 (D, H, L) for three different samples. Pinpointing the cause for lower AUC values in DFIR classifier is challenging since the dissimilarities in FT-IR and DFIR classifiers can be found at multiple stages of data collection and characteristics of the data. Considering the inherent difference in imaging modalities, further causes for divergence of the results are likely to occur due to lower SNR obtained in DFIR data, differences in pixel size and spectral step size. In terms of future application of pre-built classifiers on discrete frequency data, some of the factors outlined above such as spectral step size are easily matched to FT-IR data on which the classifier was built. Spectral matrices can be modified based on baseline and peak positions and to account for the variations in pixel size when data from different modalities needs to be matched but how the differences in pixel sizes can impact classification likely depends on the tissue and its morphology.

Specific band based detection for digital detection of fibrosis

Even though high accuracy classifiers can be developed using DFIR systems, the full potential of the system can only be realized when high speed detection can be optimized. In terms of identification of various cell types, multivariate analysis is required for disease detection and has been applied successfully in past15,33–38. Depending on the biochemistry of the tissue, we hypothesized that a single spectral feature (metric) could exist that can give a fast identification of disease in some cases. Metrics were analyzed instead of raw data since conversion of data to

metric is an effective way to reduce data while preserving spectral features15. In addition, baseline correction and normalization was implemented in metrics which is important to remove tissue thickness variation related artefacts and IR light dispersion related effects27. Specifically in case of heart tissue, we observed that fibrosis, which results from high deposition of extracellular matrix could be easily separated from myocardium by observing the contrast produced from absorbance at 1236 cm-1 peak3. Additional peaks could be of interest in generating contrast as well, and more recently, regions of fibrosis and hepatocyte populations in liver were visualized by plotting absorbance at 1656 cm-1 and 1032 cm-1 obtained on a discrete frequency imaging instrument39. In the current model, we were interested in identifying a single feature to produce contrast indicative of high ECM deposition in cardiac biopsies. We selected all 11 spectral features (metrics) that the DF-IR Bayesian classifier utilized for differentiation between myocardium and fibrosis. We then set a range of all possible values for each of these metrics by plotting the histograms of values from myocardium and fibrosis pixels. Over this range, a threshold was needed to determine whether the pixel belonged to myocardium or fibrosis based on the value of the metric. Twenty threshold values were tested for each metric and accuracy was plotted at each metric to determine the optimal threshold. Based on the maximum accuracy obtained (supplementary table 2), the metric corresponding to peak height ratio of amide III (1236cm-1) to amide II (1542 cm-1) was identified to be the top performing metric. Fine optimization of threshold was performed for this metric to identify the operating point of threshold (supplementary figure 1). The results obtained by this method (figure 4 (C, G, K)) can be compared to results obtained from the classifiers and the H&E in figure 4 (D, H, L) and the confusion matrix for this detection has been shown in table 3. As expected, the single feature based system performs worse than both FT-IR and DFIR classifiers in terms of overall accuracy, highlighting the need for multivariate analysis for accurate identification. Nevertheless, a single feature comprising of six spectral frequencies achieved an impressive 87.5% accuracy, which makes it ideal for initial, real time probing of the sample to identify tissue scarring before further analysis can be performed. Moreover, in disease states a single pixel (equivalent to a single cell) is of little meaning and the diagnosis is made by observing characteristic distribution of cells and ECM in a biopsy; which can be accomplished with the models developed here.

Multiclass detection with DFIR data

Last, we sought to examine whether multi-class classifiers can be developed with DFIR data. Here, to obtain a more comprehensive and useful model, we expanded the approach for general cardiac pathology by adding more histological states. Fibrosis is the scarring of tissue due to deposition of excess extra-cellular matrix, which can lead to reduction in functionality of heart 40,41. Increased fibrosis can lead to loss of contractile function and reserve42. Additionally, scarring causes high mechanical stiffness and diastolic dysfunction 43. Cardiac amyloid deposition is a pathological feature of advanced cardiomyopathy. Unlike conventional amyloidosis, this histopathological feature is due to breakdown products of normal or abnormal proteins called amyloids that accumulate in the heart44. These conditions can result in increasing heart stiffness and eventual deterioration of heart pumping function44. Thus, identification of cell death and protein deposition in cardiac tissue is important and can be indicative of many cardiomyopathies. In the newly expanded classifier, we looked for these tissue damage signatures in congenital heart. In the limit of the samples studied, the classifier performed robustly to identify myocardium, fibrosis, blood and cell death, which combined the classes of apoptosis, necrosis and infarction. As expected, multiclass classifier required additional information that was evident as the number of metrics needed to perform classification increased to 18 (supplementary table 3). The area under the curve of the ROC curve appeared to be lower for validation set when compared to the training set (figure 3 (vi) and (vii)) and achieved an accuracy of about 83% (table 4). There is potential to further improve classification accuracy by training on a larger dataset since patient to patient variations can have greater effects when the classifier is trained with small number of samples. As shown in figure 5, additional classes were identified by the classifier built and trained on DFIR data and showed correspondence to pathologist identified regions of cell death, red blood cells, myocardium and extracellular matrix (ECM). The accumulation of fibrous tissue in the ECM corresponded with pathologist identified regions of fibrosis. Since amyloid is also characterized by interstitial protein, the ECM signature could correspond to collagen as well as other proteins and accurate interpretation is dependent on character of the protein, spatial location and distribution. This can be easily performed on digitally classified images by employing neighboring pixel analysis towards an advanced

automated histology. We also anticipate that high speed identification of multiple histological classes can benefit from a multiclass Bayesian classifier developed specifically on DFIR data to provide reliable classification in a short time.

Discussion

In this study, we built two histologic classifiers that were trained on FT-IR and DFIR data respectively. We used a completely independent set of patients for training the FT-IR classifier which was not used for DF-IR imaging. Since patient samples used to train FT-IR and DFIR classifiers were different, we sought to compare the spectral features selected by each of these classifiers (supplementary table 1 and supplementary table 2) and study if similar biochemical information was identified in both classifiers. We observed that both classifiers utilized peaks in the 1027 cm-1 – 1040 cm-1 which could have contributions from glycogen (C-O and C-C stretching motions) and nucleic acids (phosphodiester groups and C-O stretching in ribose or deoxyribose). Both classifiers also select peaks around the 1070 cm-1 to 1090 cm-1 region which has heavy contribution of symmetric phosphate stretching from nucleic acids and additionally some stretching from glycogen C-O and C-C bonds. Therefore, even though the classifiers were constructed on two independent set of patients using two different imaging instruments, not only did the classifier provide accurate results, but also the peaks that contributed the most to differentiation between the two classes were conserved in different metric definition combinations. Interestingly, one metric was identical between the two classifiers, corresponding to peak height ratio between amide III (1236 cm-1) and amide II peak (1542 cm-1 or 1543 cm-1) with some overlap with phosphate vibration of nucleic acids. In the tissue studied, high values of this ratio were always obtained in fibrotic regions which did not have high cell density, implying that collagen and extracellular matrix proteins could be the highest contributors to this metric. The conservation of spectral features across classifiers built on different platform highlights the importance of Amide III band in tissue distinction and could possibly be the most important decision making step in differentiating between myocardium and fibrosis. This was confirmed by calculating accuracy for each of the DFIR classifier metrics towards differentiation of myocardium and fibrosis (supplementary table 2). To maximize the advantage of speed in DFIR, we confirmed that plotting a single metric of normalized Amide III absorbance at 1236

cm-1 correlated with fibrotic regions, enabling an even faster fibrosis identification protocol. The fibrosis regions identified in this manner matched with fibrosis regions recognized by the classifier. Referencing to figure 2, using six spectral bands for identification of fibrosis would be significantly faster than conventional FT-IR imaging system to obtain contrast produced in figure 4 (C, G, K). Multiclass classifier could be developed with high accuracy for classification of many other classes and utilized only a fraction of full range of frequencies. Such an approach has a potential to be further improved by adding more classes with the developments in instrumentation to improve SNR and using more number of samples for building a robust classification system. The aim of this paper was to introduce direct application of new generation IR based imaging and staining technology towards digital pathology. To that end, we have omitted detailed discussion about the instrumentation in terms of spatial and spectral noise and SNR which are ongoing. These will be addressed in details in future work.

Conclusions

This study demonstrates a DFIR imaging approach for rapid identification of complex histopathological states in the heart and, in particular, the rapid identification of tissue scarring. Classification was achieved by using a limited set of frequencies; this reduction in data acquired was the factor responsible for the speed advantage. We observed that the classifier developed on FT-IR imaging data performed with high accuracy on DFIR imaging data. This is significant since this may enable us to apply previously built FT-IR imaging data based classifiers on DFIR imaging data at high speeds by identifying specific spectral features of importance. In addition, it offers a way to get high accuracy in digital histopathology using DFIR data. Despite low SNR data currently recorded with the DFIR system, the DFIR imaging data based classifier could also identify tissue types correctly with high accuracy. While this dataset is not comprehensive for all cardiomyopathies, further work could ensure high accuracy and expansion of classifier. There is also significant potential for faster triaging of samples. Fast identification using IR spectroscopic imaging is becoming a reality with new imaging instruments and the DFIR approach, which could permit real-time visualization of some information with specific regions being probed in greater spectral detail. Further, the same setup can lead to imaging at different pixel sizes. This diversity in spectral and spatial sampling, within the same imaging step, presents novel

opportunities for optimization. Clinically useful images comparable to FT-IR imaging can be obtained significantly more rapidly, paving the way for this approach to be clinically translated for real-time pathology.

Acknowledgements

The authors would like to thank Agilent Technologies Inc. for providing the DFIR imaging instrument during the course of this study. We would also like to thank Kevin Yeh for informative discussions about DFIR data analysis. We thank the Beckman Foundation for a Beckman Institute graduate student award to S.T.

Figures and Tables

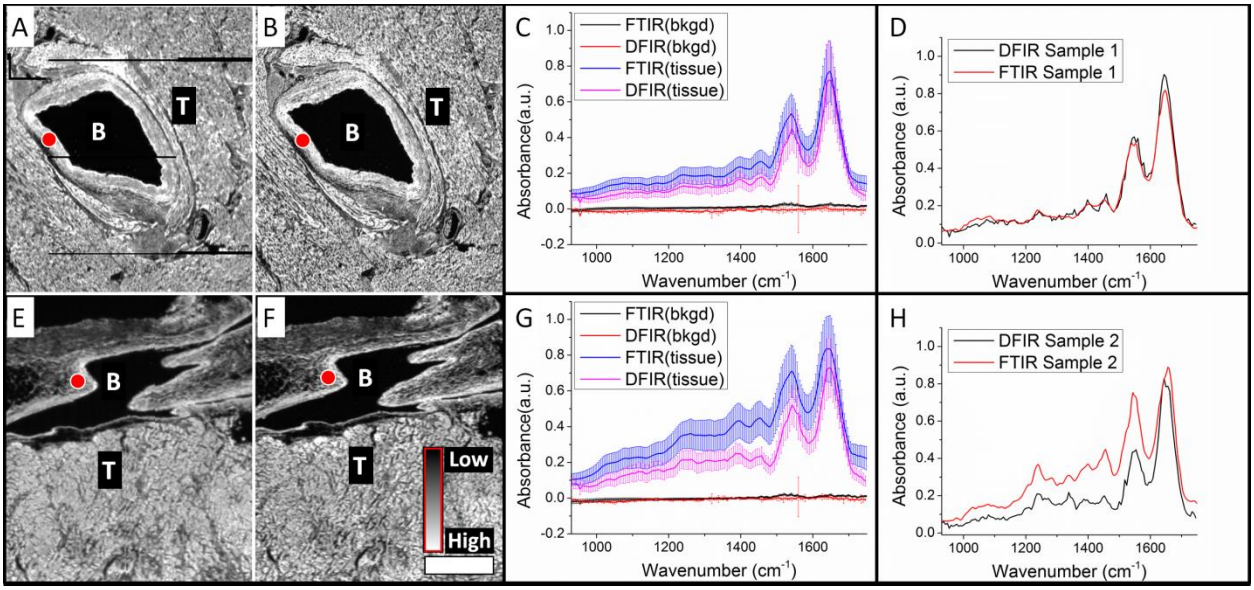

Figure 11. Comparison of images and spectra obtained from FT-IR and DFIR instruments for two different patient samples. Images obtained using (A, E) FT-IR imaging data (B, F) DFIR imaging data using the absorbance at 1652 cm^{-1}. The shaded region represents non-normalized amide I intensity as gray scale image. Scale bar represents 500µm (C, G) Average spectra obtained for FT-IR and DFIR images for background and tissue regions marked as B and T in the images from more than 5000 pixels over similar sized regions. (D, H) Spectra obtained at specific points in DFIR and FT-IR images at regions marked in images as red dots.

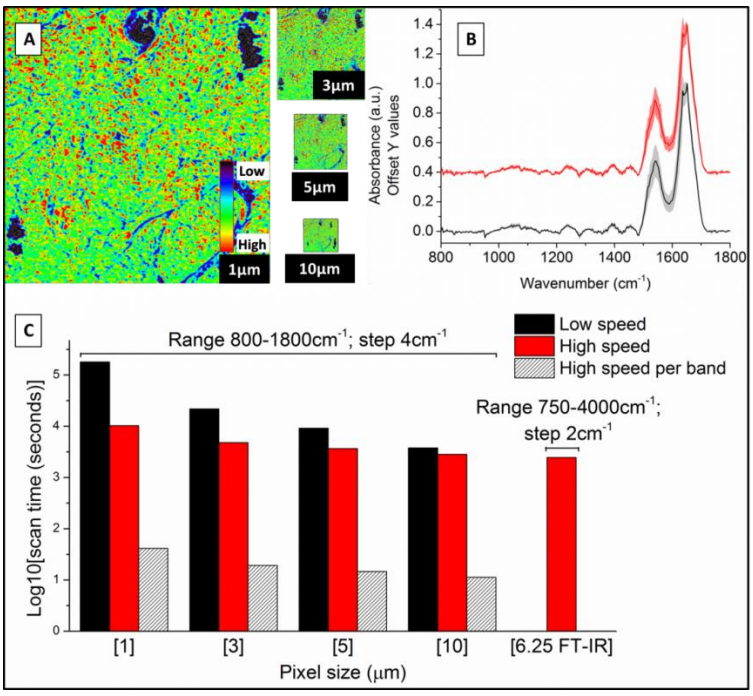

Figure 12. Imaging with DFIR instrumentation. (A) Image of myocardium collected at different pixel sizes. Every box is image area of 2.02 mm x 1.94 mm at shown pixel size to demonstrate the relative data sizes, obtained using the absorbance at 1656 cm^{-1} and plotted as color bar shown in (A). (B) Absorption spectra show data collected at high speed (red) and low speed (black) on DFIR imaging instrument. (C) Time required to image plotted for various pixel sizes for the scan area of 2.5 mm^2

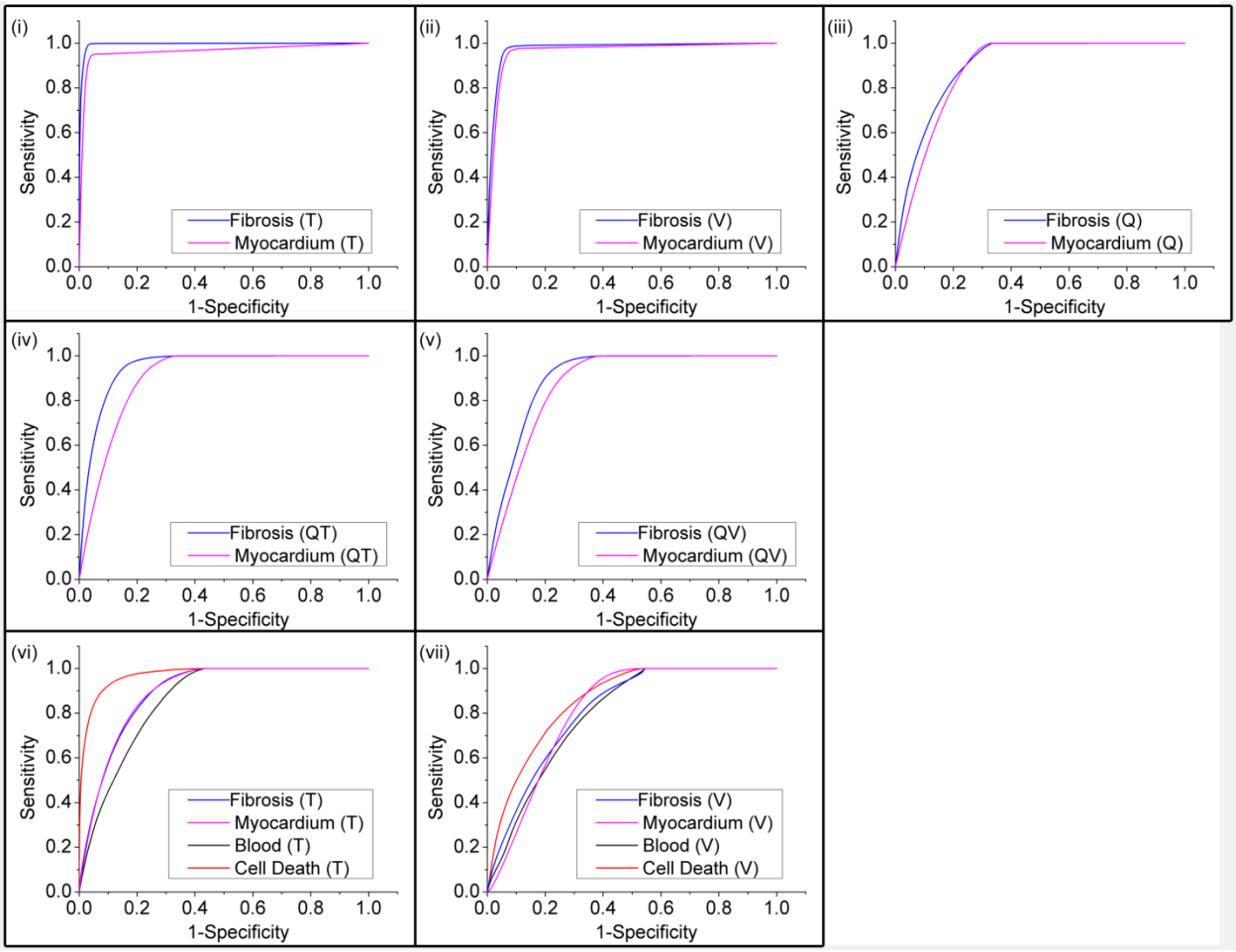

Figure 13. Receiver operating characteristic (ROC) curves for classifiers. (i) Training on FT-IR imaging dataset (ii) Validation of FT-IR imaging based classifier on FT-IR imaging dataset (iii) Application of FT-IR imaging based classifier on DFIR imaging dataset (iv) Training on DFIR imaging dataset (v) Validation of DFIR imaging based classifier on DFIR imaging dataset (vi) Training of multiclass classifier on DFIR imaging dataset (vii) Validation of multiclass classifier on DFIR imaging dataset

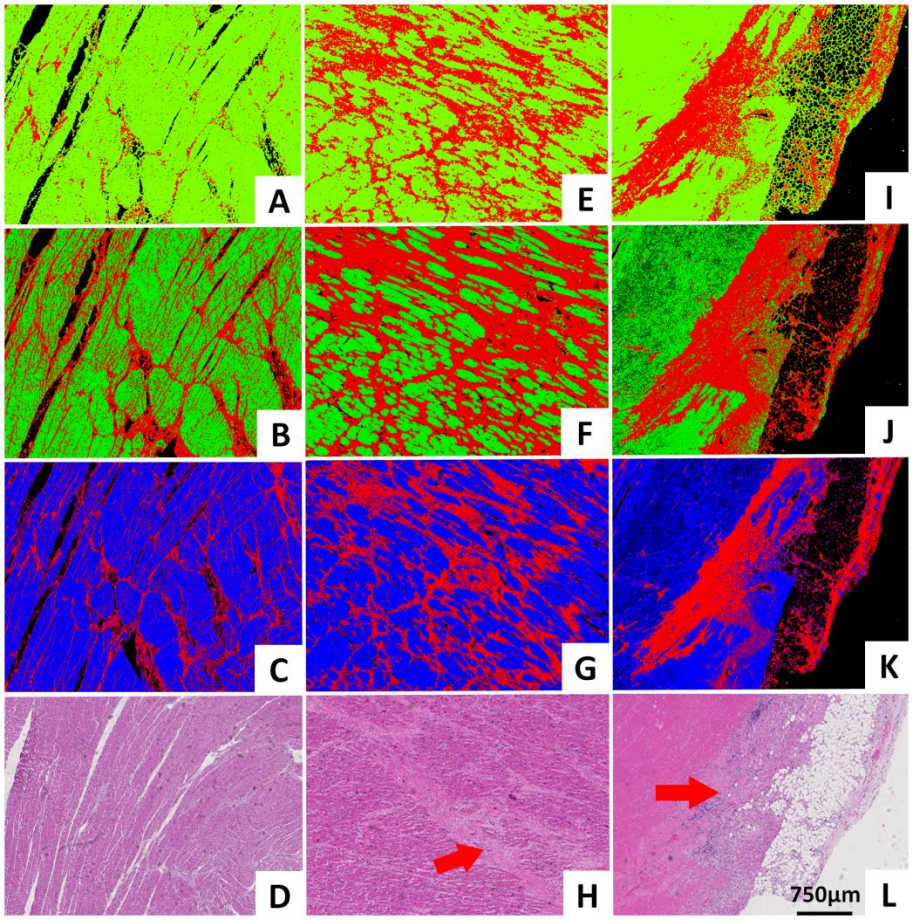

Figure 14: Classification results shown for DFIR images of three different samples. (A, E, I) Classifier developed on FT-IR data. (B, F, J) Classifier developed on DFIR data. (C, G, K) Single metric identification of fibrosis. Red regions in all the IR colored images are fibrosis. Corresponding H&E images are shown in (D, H and L). Red arrows indicate the regions identified by the pathologist as fibrosis.

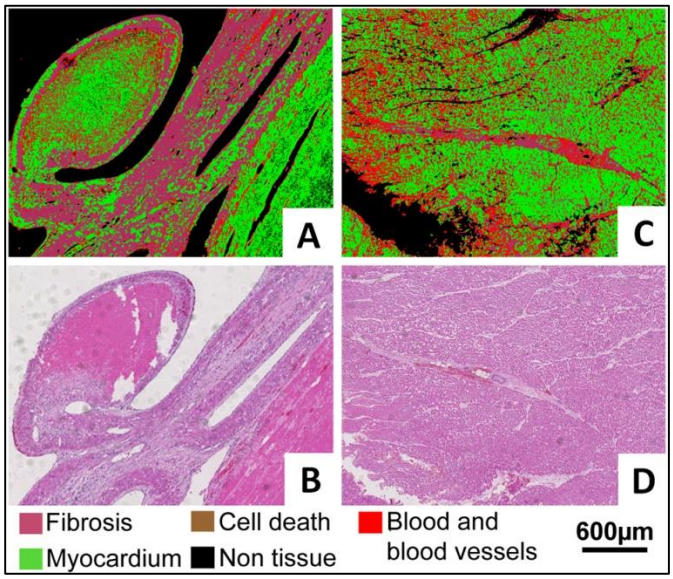

Figure 15: Classification results of multiclass classifier on DFIR images of two different samples. (A, C) Classified images showing Fibrosis, Myocardium, Cell death, Blood and blood vessels and Non-tissue regions. (B,D) Corresponding H&E.

Table 6: Confusion matrix for FT-IR imaging based classifier applied on DFIR imaging dataset

	Ground Truth (Percent)		
Class	**Myocardium**	**Fibrosis**	**Total**
Unclassified	0.01	**0**	0
Myocardium	96.14	18.65	87.43
Fibrosis	3.85	81.35	12.57
Total	100	100	100
		Overall Accuracy	**94.42%**

Table 7: Confusion matrix for DFIR imaging based classifier applied on DFIR imaging dataset

	Ground Truth (Percent)		
Class	**Myocardium**	**Fibrosis**	**Total**
Unclassified	0	0	0
Myocardium	91.4	12.22	82.5
Fibrosis	8.6	87.78	17.5
Total	100	100	100
		Overall Accuracy	**90.99%**

Table 8: Confusion matrix for specific band based detection

	Ground Truth (Percent)		
Class	**Myocardium**	**Fibrosis**	**Total**
Myocardium	94.02	34.09	80.12
Fibrosis	5.98	65.91	19.88
Total	100	100	100
		Overall Accuracy	**87.50%**

Table 9: Confusion matrix for multiclass DFIR imaging based classifier

	Ground Truth (Percent)				
Class	**Blood**	**Cell death**	**Fibrosis**	**Myocardium**	**Total**
Blood	57.93	10.52	21.85	1.97	10.95
Cell death	0.03	3.67	0.03	0.01	0.08
Fibrosis	33.05	8.05	66.29	6.61	24.49
Myocardium	8.99	77.76	11.84	91.41	64.48
Total	100	100	100	100	100
				Overall Accuracy	**82.87%**

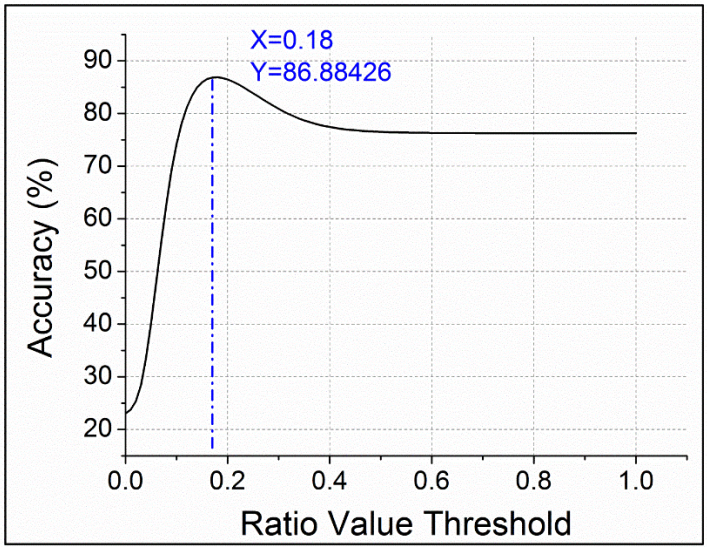

Figure 16: Optimal threshold identification. Shown here is the threshold identification for peak height ratio of 1236 cm^{-1} and 1542 cm^{-1} after fine tuning the ratio value threshold.

Table 10. Metrics used in FT-IR imaging based classifier in the order of addition

Metric type	Feature 1	Feature 2
Peak height ratio	1389 cm^{-1}	1236 cm^{-1}
Peak area to height ratio	1274 cm^{-1} to 1543 cm^{-1}	1652 cm^{-1}
Peak height ratio	1239cm^{-1}	1543 cm^{-1}
Peak height ratio	1339 cm^{-1}	1543 cm^{-1}
Peak height ratio	1236 cm^{-1}	1543 cm^{-1}
Peak height ratio	1389 cm^{-1}	1452 cm^{-1}
Center of gravity	1482 cm^{-1}	1594 cm^{-1}
Peak area to height ratio	1324 cm^{-1} to 1358 cm^{-1}	1652 cm^{-1}
Peak height ratio	1405 cm^{-1}	1236 cm^{-1}
Peak area to height ratio	1482 cm^{-1} to 1594 cm^{-1}	1652 cm^{-1}
Peak height ratio	1027 cm^{-1}	1236 cm^{-1}
Center of gravity	1048 cm^{-1}	1070 cm^{-1}
Peak height ratio	1389 cm^{-1}	1065 cm^{-1}

Table 11: Metrics used in DFIR imaging based classifier in the order of addition, accuracy percentage is the accuracy obtained at each metric individually at optimized threshold values

Metric type	Feature 1	Feature 2	Accuracy (%)
Peak height ratio	1038 cm^{-1}	1542 cm^{-1}	78.821
Peak area to height ratio	1482 cm^{-1} to 1590 cm^{-1}	1038 cm^{-1}	70.09
Peak area to height ratio	996 cm^{-1} to 1140 cm^{-1}	1542 cm^{-1}	79.712
Peak height ratio	1236 cm^{-1}	1542 cm^{-1}	86.46
Peak area to height ratio	1482 cm^{-1} to 1590 cm^{-1}	1236 cm^{-1}	76.24
Peak area to height ratio	1182 cm^{-1} to 1290 cm^{-1}	1542 cm^{-1}	81.831
Peak area to height ratio	1482 cm^{-1} to 1710 cm^{-1}	1236 cm^{-1}	76.203
Peak height ratio	1236 cm^{-1}	1650 cm^{-1}	85.185
Peak area to height ratio	1182 cm^{-1} to 1290 cm^{-1}	1650 cm^{-1}	80.239
Peak height ratio	1074 cm^{-1}	1650 cm^{-1}	72.031
Peak area to height ratio	1482 cm^{-1} to 1590 cm^{-1}	1020 cm^{-1}	53.126

Table 12: Metrics used in multi-class DFIR imaging based classifier in the order of addition

Metric type	Feature 1	Feature 2
Peak area to height ratio	1362 cm^{-1} to 1428 cm^{-1}	1650 cm^{-1}
Peak area to height ratio	1482 cm^{-1} to 1590 cm^{-1}	1038 cm^{-1}
Peak area to area ratio	1428 cm^{-1} to 1482 cm^{-1}	1590 cm^{-1} to 1710 cm^{-1}
Peak area to height ratio	1482 cm^{-1} to 1710 cm^{-1}	1464 cm^{-1}
Peak height ratio	1038 cm^{-1}	1398 cm^{-1}
Peak area to height ratio	1482 cm^{-1} to 1710 cm^{-1}	1236 cm^{-1}
Peak area to area ratio	1362 cm^{-1} to 1428 cm^{-1}	1590 cm^{-1} to 1710 cm-1
Peak height ratio	1236 cm^{-1}	1464 cm^{-1}
Peak area to height ratio	1482 cm^{-1} to 1590 cm^{-1}	1236 cm^{-1}
Peak height ratio	1482 cm^{-1}	1650 cm^{-1}
Peak area to area ratio	1482 cm^{-1} to 1590 cm^{-1}	1590 to 1710 cm^{-1}
Peak area to height ratio	1482 cm^{-1} to 1590 cm^{-1}	1020 cm^{-1}
Peak area to area ratio	1362 cm^{-1} to 1482 cm^{-1}	1590 cm^{-1} to 1710 cm^{-1}
Peak height ratio	1020 cm^{-1}	1398 cm^{-1}
Peak area to height ratio	996 cm^{-1} to 1140 cm^{-1}	1542 cm^{-1}
Peak area to area ratio	996 cm^{-1} to 1140 cm^{-1}	1590 cm^{-1} to 1710 cm^{-1}
Peak area to height ratio	1362 cm^{-1} to 1428 cm^{-1}	1020 cm^{-1}
Peak area to height ratio	1482 cm^{-1} to 1710 cm^{-1}	1038 cm^{-1}

References

1. Mozaffarian D, Benjamin EJ, Go AS, et al. Heart Disease and Stroke Statistics-2015 Update: A Report From the American Heart Association. Circulation 2014;131(4):e29-322. doi:10.1161/CIR.0000000000000152.

2. Mayerich D, Walsh MJ, Kadjacsy-Balla A, Ray PS, Hewitt SM, Bhargava R. Stain-less staining for computed histopathology. TECHNOLOGY 2015:1-5. doi:10.1142/S2339547815200010.

3. Tiwari S, Reddy VB, Bhargava R, Raman J. Computational chemical imaging for cardiovascular pathology: chemical microscopic imaging accurately determines cardiac transplant rejection. PLoS One 2015;10(5):e0125183. doi:10.1371/journal.pone.0125183.

4. Holton SE, Bergamaschi A, Katzenellenbogen BS, Bhargava R. Integration of molecular profiling and chemical imaging to elucidate fibroblast-microenvironment impact on cancer cell phenotype and endocrine resistance in breast cancer. PLoS One 2014;9(5):e96878. doi:10.1371/journal.pone.0096878.

5. Smolina M, Goormaghtigh E. Infrared imaging of MDA-MB-231 breast cancer cell line phenotypes in 2D and 3D cultures. Analyst 2015;140(7):2336-43. doi:10.1039/c4an01833h.

6. Tiwari S, Zong X, Holton SE, Prasanth K V., Bhargava R. Fourier transform infrared (FT-IR) spectroscopy and imaging of the nucleus to characterize DNA contributions in different phases of the cell cycle. In: Gimi B, Molthen RC, eds. SPIE Medical Imaging. International Society for Optics and Photonics; 2015:941720. doi:10.1117/12.2082347.

7. Krafft C, Salzer R, Soff G, Meyer-Hermann M. Identification of B and T cells in human spleen sections by infrared microspectroscopic imaging. Cytom. Part A 2005;64(February):53-61. doi:10.1002/cyto.a.20117.

8. Lasch P, Pacifico A, Diem M. Spatially resolved IR microspectroscopy of single cells. Biopolymers 2002;67(4-5):335-8. doi:10.1002/bip.10095.

9. Ellis DI, Goodacre R. Metabolic fingerprinting in disease diagnosis: biomedical applications of infrared and Raman spectroscopy. Analyst 2006;131(8):875-85. doi:10.1039/b602376m.

10. Petibois C, Drogat B, Bikfalvi A, Déléris G, Moenner M. Histological mapping of biochemical changes in solid tumors by FT-IR spectral imaging. FEBS Lett. 2007;581:5469-5474. doi:10.1016/j.febslet.2007.10.052.

11. Großerueschkamp F, Kallenbach-Thieltges A, Behrens T, et al. Marker-free automated histopathological annotation of lung tumour subtypes by FTIR imaging. Analyst 2015;140(7):2114-20. doi:10.1039/c4an01978d.

12. Li X, Li Q-B, Zhang G-J, et al. Identification of colitis and cancer in colon biopsies by Fourier Transform Infrared spectroscopy and chemometrics. ScientificWorldJournal. 2012;2012:936149. doi:10.1100/2012/936149.

13. Mackanos M a., Contag CH. FTIR microspectroscopy for improved prostate cancer diagnosis. Trends Biotechnol. 2009;27:661-663. doi:10.1016/j.tibtech.2009.09.001.

14. Kwak JT, Kajdacsy-Balla A, Macias V, Walsh M, Sinha S, Bhargava R. Improving Prediction of Prostate Cancer Recurrence using Chemical Imaging. Sci. Rep. 2015;5:8758. doi:10.1038/srep08758.

15. Bhargava R, Fernandez DC, Hewitt SM, Levin IW. High throughput assessment of cells and tissues: Bayesian classification of spectral metrics from infrared vibrational spectroscopic imaging data. Biochim. Biophys. Acta 2006;1758(7):830-45. doi:10.1016/j.bbamem.2006.05.007.

16. Kwak JT, Reddy R, Sinha S, Bhargava R. Analysis of variance in spectroscopic imaging data from human tissues. Anal. Chem. 2012;84(2):1063-9. doi:10.1021/ac2026496.

17. Kole MR, Reddy RK, Schulmerich M V, Gelber MK, Bhargava R. Discrete frequency infrared microspectroscopy and imaging with a tunable quantum cascade laser. Anal. Chem. 2012;84(23):10366-72. doi:10.1021/ac302513f.

18. Yeh K, Kenkel S, Liu J-N, Bhargava R. Fast Infrared Chemical Imaging with a Quantum Cascade Laser. Anal. Chem. 2015;87(1):485-493. doi:10.1021/ac5027513.

19. Kodali AK, Schulmerich M, Ip J, Yen G, Cunningham BT, Bhargava R. Narrowband Midinfrared Reflectance Filters Using Guided Mode Resonance. Anal. Chem. 2010;82(13):5697-5706. doi:10.1021/ac1007128.

20. Brandstetter M, Koch C, Genner A, Lendl B. Measures for optimizing pulsed EC-QC laser spectroscopy of liquids and application to multi-analyte blood analysis. In: Razeghi M, Tournié E, Brown GJ, eds. SPIE OPTO. International Society for Optics and Photonics; 2013:89931U. doi:10.1117/12.2038585.

21. Kölhed M, Haberkorn M, Pustogov V, et al. Assessment of quantum cascade lasers as mid infrared light sources for measurements of aqueous solutions. Vib. Spectrosc. 2002;29(1-2):283-289.

22. Kröger N, Egl A, Engel M, et al. Quantum cascade laser-based hyperspectral imaging of biological tissue. J. Biomed. Opt. 2014;19(11):111607. doi:10.1117/1.JBO.19.11.111607.

23. Brandstetter M, Volgger L, Genner A, Jungbauer C, Lendl B. Direct determination of glucose, lactate and triglycerides in blood serum by a tunable quantum cascade laser-based mid-IR sensor. Appl. Phys. B 2012;110(2):233-239. doi:10.1007/s00340-012-5080-z.

24. Bassan P, Weida MJ, Rowlette J, Gardner P. Large scale infrared imaging of tissue micro arrays (TMAs) using a tunable Quantum Cascade Laser (QCL) based microscope. Analyst 2014;139(16):3856-9. doi:10.1039/c4an00638k.

25. Pilling MJ, Henderson A, Bird B, Brown MD, Clarke NW, Gardner P. High-throughput quantum cascade laser (QCL) spectral histopathology: a practical approach towards clinical translation. Faraday Discuss. 2016. doi:10.1039/c5fd00176e.

26. Tiwari S, Raman J, Reddy V, Dawson M, Bhargava R. Translation of infrared chemical imaging for cardiovascular evaluation. In: Mahadevan-Jansen A, Petrich W, eds. SPIE BiOS. International Society for Optics and Photonics; 2016:97040X. doi:10.1117/12.2230004.

27. Martin FL, Kelly JG, Llabjani V, et al. Distinguishing cell types or populations based on the computational analysis of their infrared spectra. Nat. Protoc. 2010;5:1748-1760. doi:10.1038/nprot.2010.133.

28. Baker MJ, Trevisan J, Bassan P, et al. Using Fourier transform IR spectroscopy to analyze biological materials. Nat. Protoc. 2014;9(8):1771-91. doi:10.1038/nprot.2014.110.

29. Tiwari S, Bhargava R. Extracting knowledge from chemical imaging data using computational algorithms for digital cancer diagnosis. Yale J. Biol. Med. 2015;88(2):131-43.

30. Mayerich D, van Dijk T, Walsh MJ, Schulmerich M V, Carney PS, Bhargava R. On the importance of image formation optics in the design of infrared spectroscopic imaging systems. Analyst 2014;139(16):4031-6. doi:10.1039/c3an01687k.

31. Mattson EC, Unger M, Clède S, et al. Toward optimal spatial and spectral quality in widefield infrared spectromicroscopy of IR labelled single cells. Analyst 2013;1(Scheme 1):19-22. doi:10.1039/c3an00383c.

32. Reddy RK, Bhargava R. Accurate histopathology from low signal-to-noise ratio spectroscopic imaging data. Analyst 2010;135(11):2818-25. doi:10.1039/c0an00350f.

33. Ollesch J, Heinze M, Heise HM, Behrens T, Brüning T, Gerwert K. It's in your blood: spectral biomarker candidates for urinary bladder cancer from automated FTIR spectroscopy. J. Biophotonics 2014;7(3-4):210-21. doi:10.1002/jbio.201300163.

34. Owens GL, Gajjar K, Trevisan J, et al. Vibrational biospectroscopy coupled with multivariate analysis extracts potentially diagnostic features in blood plasma/serum of ovarian cancer patients. J. Biophotonics 2014;7(3-4):200-9. doi:10.1002/jbio.201300157.

35. Bonnier F, Rubin S, Ventéo L, et al. In-vitro analysis of normal and aneurismal human ascending aortic tissues using FT-IR microspectroscopy. Biochim. Biophys. Acta - Biomembr. 2006;1758:968-973. doi:10.1016/j.bbamem.2006.05.018.

36. Wang L, Chapman J, Palmer R a., van Ramm O, Mizaikoff B. Classification of atherosclerotic rabbit aorta samples by mid-infrared spectroscopy using multivariate data analysis. J. Biomed. Opt. 2007;12(April 2007):24006. doi:10.1117/1.2714030.

37. German MJ, Hammiche A, Ragavan N, et al. Infrared spectroscopy with multivariate analysis potentially facilitates the segregation of different types of prostate cell. Biophys. J. 2006;90(May):3783-3795. doi:10.1529/biophysj.105.077255.

38. Travo A, Piot O, Wolthuis R, et al. IR spectral imaging of secreted mucus: a promising new tool for the histopathological recognition of human colonic adenocarcinomas. Histopathology 2010;56(7):921-31. doi:10.1111/j.1365-2559.2010.03563.x.

39. Sreedhar H, Varma VK, Gambacorta F V., Guzman G, Walsh MJ. Infrared spectroscopic imaging detects chemical modifications in liver fibrosis due to diabetes and disease. Biomed. Opt. Express 2016;7(6):2419. doi:10.1364/BOE.7.002419.

40. Weber KT. Fibrosis and hypertensive heart disease. Curr. Opin. Cardiol. 2000;15(4):264-72.

41. Krenning G, Zeisberg EM, Kalluri R. The origin of fibroblasts and mechanism of cardiac fibrosis. J. Cell. Physiol. 2010;225(3):631-7. doi:10.1002/jcp.22322.

42. Ertl G, Frantz S. Healing after myocardial infarction. Cardiovasc. Res. 2005;66(1):22-32. doi:10.1016/j.cardiores.2005.01.011.

43. Chaturvedi RR, Herron T, Simmons R, et al. Passive stiffness of myocardium from congenital heart disease and implications for diastole. Circulation 2010;121(8):979-88. doi:10.1161/CIRCULATIONAHA.109.850677.

44. Quarta CC, Kruger JL, Falk RH. Cardiac amyloidosis. Circulation 2012;126(12):e178-82. doi:10.1161/CIRCULATIONAHA.111.069195.

SUMMARY

In this work, we have developed infrared chemical imaging based approach towards digital pathology of cardiac biopsy samples. We first applied supervised Bayesian classification approach to identify lymphocytes, fibrosis in endocardium, fibrosis in myocardium, myocardium and endocardium with sensitivity of greater than 95% for all classes except endocardium at 90% specificity, while the sensitivity of endocardium was also at least 85%. This is the first demonstration of application of Fourier transform infrared spectroscopic imaging towards cardiac histology and is significant in establishing that the histological classes identified in endomyocardial biopsy samples have intrinsic chemical contrast. We also tested the performance of this classifier on low spatial resolution data collected at 25μm to assess if high speed detection could be achieved. While probability of detection was high for myocardium and average for lymphocytes, the classifier could not distinguish between other classes well.

Following our previous attempts at developing a protocol for high speed histology, the next approach that we tested was using quantum cascade laser based discrete frequency instruments. This enabled us to collect data at high speed without compromising the spatial resolution. We first tested if the data collected in DFIR mode, which had lower signal to noise compared to FT-IR data could be used for differentiation of histological classes based on spectral features. We observed that the unsupervised clustering detected similar regions in data collected on both DFIR and FT-IR instruments, indicating that the spectral differences that led to differentiation of classes in FT-IR were preserved in DFIR data despite low SNR.

Next, we tested different approaches to develop high accuracy classification models for DFIR data. We first applied the classifiers built previously on FT-IR data on data collected in DFIR mode. This classifier performed well on discrete frequency data, confirming the premise that Bayesian classification can identify specific spectral features necessary and sufficient for identification of histological classes. We also developed a Bayesian classifier on DFIR data to assess the highest accuracy achieved in classification. Given the lower signal to noise ratio obtained in discrete frequency mode, it was expected that the accuracy would be lower for the classifier developed on DFIR data. This was confirmed by calculating the accuracy of final

classification, which dropped to about 91%. This accuracy lowered further when a multi-class classifier was developed on DF-IR data. We anticipate the issue of lower accuracy of classifiers developed on DF-IR data can be resolved with using a larger number of samples for training the classifiers, and applying noise correction algorithms.

Finally, we were interested to see if the speed advantage of discrete frequency approach could be realized to its full potential by using a single metric based identification. We aimed to identify fibrosis in the myocardium which is indicative of tissue damage due to a number of factors such as immune response and myocardium damage and can be indicative of loss of function of heart muscle. We tested all the metrics utilized in Bayesian classifier for differentiation of fibrosis from myocardium, and chose the metric with highest accuracy of differentiation. This metric was found to achieve an accuracy of 87.5% for the differentiation of fibrosis from myocardium. While the use of discrete frequency mode as compared to FT-IR mode can lower the time required to image by 20-folds, this result can further reduce the time required by a factor of 10, making this technology practical and relevant on clinical scale. In the bigger picture, this work will be useful in developing probe based technology by direct implementation of results obtained from this work for a high speed detection of fibrosis. In addition, with high speed imaging being made possible by quantum cascade laser technology, this work contributes significantly towards high speed digital histopathology of cardiac tissue.